

Elsevier Editorial System(tm) for Journal of
Natural Gas Science & Engineering
Manuscript Draft

Manuscript Number: JNGSE-D-18-01722R1

Title: Numerical modeling of CO₂ fracturing by the phase field approach

Article Type: Full Length Article

Keywords: CO₂ fracturing; CO₂ fluid flow; phase field

Corresponding Author: Professor Yongxing Shen, Ph.D.

Corresponding Author's Institution: Shanghai Jiao Tong University

First Author: Mostafa Mollaali

Order of Authors: Mostafa Mollaali; Vahid Ziae Rad, Ph.D.; Yongxing Shen, Ph.D.

Abstract: We propose a phase field model to simulate CO₂ fracturing under an isothermal condition. We take advantage of the ability of the phase field approach in predicting fracture initiation and branching, and also to avoid tracking the fracture path. We model the CO₂ as a compressible fluid by modifying Darcy's law. In particular, we assume the permeability is correlated to the phase field value by an exponential function. The dependence of the CO₂ density as a function of the pressure is captured by the Span-Wagner equation of state. The computed breakdown pressure values show good agreement with analytical solutions and experimental results.

Research Data Related to this Submission

There are no linked research data sets for this submission. The following reason is given:

Data will be made available on request

Response to reviewer comments on ‘Numerical modeling of CO₂ fracturing by the phase field approach’

Mostafa Mollaali^a, Vahid Ziae-Rad^b, Yongxing Shen^{a,*}

^a*University of Michigan – Shanghai Jiao Tong University Joint Institute, Shanghai Jiao Tong University, Shanghai, China*

^b*Faculty of Civil, Water and Environmental Engineering, Shahid Beheshti University, Tehran, Iran*

We thank the reviewers for their constructive comments to render the manuscript with higher quality. Below we first respond to each of the comments with the original comments italicized, then summarize the major changes of the manuscript. However, since this is an extensive revision, we will not provide a detailed list of changes since that would mean an extensive repetition of the text. Here we only bring to the editor’s and reviewers’ attention that we have merged the former Appendix A into the first three subsections of Section 4 to make the latter following an order from simple examples to complicated ones. Also note that **all other changes in the manuscript** are marked in blue.

Comments from Reviewer #1

In overall, the manuscript is well written. I would recommend this manuscript for further consideration if the authors make the following revisions:

The nomenclature should be consistent with SPE nomenclature, for example v should be used for velocity instead of q , l should be used for length instead of σ .

We appreciate the reviewer’s positive comment. Following the SPE nomenclature, now we have substituted v for q . Following the convention of the phase field for fracture community, we reserve ℓ for the regularization length scale. Note that σ is nowhere used for length but for the *in situ* stress.

When CO₂ flow in the fracture and in rock, there are more than one phase because formation fluids also flow, hence the formulation should be for at least two phase.

It is true that including more phases would lead to a more realistic model. Moreover, our formulation for CO₂ as a compressible fluid is applicable to more than one phase with minimal changes. This being said, however, there are cases

*Corresponding author

Email address: yongxing.shen@sjtu.edu.cn (Yongxing Shen)

in which one phase is sufficient, and which is the scope of the proposed method in its current form, because the more complex the model, the more difficult to verify and validate. So at this stage, we confine ourselves to the simpler case of one phase to carefully verify the model, and generalization to more phases can be a future step. More precisely, it will be assumed that CO₂ is in its supercritical state, and as the shale is a deep reservoir, the size of the fluid lag is negligible. In the revision we added the limitation of the proposed method at the end of Section 2.

Please use a consistent color set for all figures, scale in some figures changes white to black while others change from blue to white.

We have edited Figure 1. The color bars are now from blue to red everywhere. It is also worth mentioning that in the current Section 4.1 the initial cracks are explicitly imposed, so that in the deformed configuration in Figure 4 they appear as lines in the color of the background (in the normal case white). See the caption of Figure 4.

Please include a short paragraph to show how d and α_k (Eq. 9) are determined?

The phase field d is the key parameter in the phase field approach. It is obtained by minimizing (3), holding other fields fixed, which leads to the weak form, now numbered (A.1b). The solution procedure is given in Section 3, in which it is elaborated how the phase field d is solved while coupled to \mathbf{u} and p . The current Appendix A.1 gives the discretized form for the residual vectors and tangent stiffness matrices for solving d as well as \mathbf{u} .

The parameter α_k is a parameter to input. We have expanded the paragraph surrounding Equation (9) to explain this point.

Please use more close to reservoir condition for input data. The tensile strength in Tab. 1 is very high for the rock with that Young's modulus. The initial pressure is rather too low.

Since we aimed to verify our results with Wang *et al.* [1], the selected input data are in accordance with this reference. Also, all mechanical input data are approximately within the range proposed for the shale in a few references. See, e.g., Table 1 for a comparison between our input data with the suggested mechanical properties for the shale by Eseme *et al.* [2], in which the authors reviewed literature on the mechanical properties of oil shales. Also, the initial pressure is in accordance with [1].

Table 1: Mechanical properties of rich shale from the Western US.

| Property | Symbol | Unit | Values from [2] | Our values |
|------------------|------------|------|-----------------|------------|
| Young's modulus | E | GPa | 4.5 ± 0.5 | 6 |
| Poisson's ratio | ν | — | 0.35 | 0.34 |
| Tensile strength | σ_t | MPa | 9.5 ± 1.5 | 11 |

Please include all necessary inputs for the simulation to allow other people to duplicate the job if needed. There is no data related to in-situ stresses. Although, they are not in the equation but they are the boundary condition.

We found we missed in one place the values of *in situ* stresses, which we have added on p. 22, l. 341. We believe now all other input data and the algorithm are sufficient for reproducing the results.

More numerical simulation or case studies may be needed and a comparison with other models may be useful to show the innovation of this model.

What makes the phase field an attractive approach can be attributed to its convenience in simulating complex fracture processes, including crack initiation, propagation, branching and merging. Compared to discrete crack descriptions, the phase field approaches avoid tracking the complicated crack geometry; instead, the crack evolution is a natural outcome of the numerical solution to a constrained optimization problem. Thus, it significantly decreases the implementation difficulty, especially when dealing with 3D problems. To illustrate this major advantage, in this version, we added two more application examples to the manuscript; (1) increasing pressure leading to joining cracks, as Section 4.4, and (2) interaction between CO₂-driven fractures and inclined natural fractures, as Section 4.6. Both examples result in complicated crack topologies. At the end of Section 2, we also added a paragraph to discuss the innovation of the current model.

We need more section to discuss the advantage of the model compared to other approaches.

We added one paragraph to the end of Section 2 to discuss the advantages as well as limitations of the current approach.

Comments from Reviewer #2

This paper presents a very novel approach to model the CO₂ fracturing process. I think this topic is very new and definitely worth digging into. The authors have presented enough details about the fundamentals of the solution, and overall I think this paper is very well laid out. I have following minor suggestions for further improvement:

1. *One main concern is that this paper seems too mathematical.*

We appreciate the reviewer's positive comments. Since the objective of this paper is to propose a *numerical* model for CO₂ fracturing, we had to provide necessary formulas in a way that readers can reproduce our results.

The layout of the manuscript could benefit from more description about the application of the methodology.

We added two more application examples to the manuscript; (1) increasing pressure leading to joining cracks, as Section 4.4, and (2) interaction between CO₂-driven fractures and inclined natural fractures, as Section 4.6.

2. The validation is not very clear to me. The author presented three verifications, but are they trying to prove the validity of the proposed method? Honestly I didn't recognize the method that was used for validation. Is it a well-established analytic solution, or results from well-established simulation? I would strongly recommend re-write the validation part.

Yes, we were trying to prove the validity of the proposed method in the former Appendix A, which is now Sections 4.1 – 4.3. In these three sets of examples, we compare our method against exact or otherwise well-established solutions for verification. See Table 2 for a summary of the requested information by the reviewer. In addition, we made some minor edits to these sections to clarify these issues.

Table 2: Summary of the verification examples.

| Section in the revised manuscript | Reference solution | Type |
|-----------------------------------|---------------------------|------------|
| 4.1 | Miehe <i>et al.</i> [3] | Numerical |
| 4.2 | Detourneau and Cheng [4] | Analytical |
| 4.3 | Sneddon and Lowengrub [5] | Analytical |

3. What is the limitation of the current method?

The limitation is the rather simple model for the gas flow and permeability in shale media. We added a summary of the limitations as well as the advantages at the end of Section 2.

It is not very clear to me that whether this method is application to traditional water based fracking or not.

The phase field approach has already been applied to water based fracking by multiple authors, see e.g., [6, 7, 8, 9, 10, 11, 12, 13].

And if so, what is the advantage of the current approach?

The advantage of the current approach is the generalization to CO_2 fracturing. In the paper at hand, we propose a phase field model to consider CO_2 as a compressible fracturing fluid under the isothermal condition, as the first step towards such modeling. More precisely, the CO_2 density varies significantly with pressure, which is captured by the Span-Wagner equation of state [14]. The computed values show good agreement with analytical solutions and experimental results.

Comments from Reviewer #3

The paper tries to use phase field method to model CO_2 fracturing. Some assumptions used in governing equations are not supported with the theory of poroelasticity. Hydraulic fracturing or CO_2 fracturing involves strongly coupled processes. But the authors verify their model through non-coupled examples.

The coupled behaviors about pressure and aperture evolutions are not demonstrated. This makes the correctness of the model in doubt. I recommend resubmission of the paper after the model is correctly verified through asymptotic analytical solutions for hydraulic fracturing. Without correctly verifying the coupled model, I cannot recommend the acceptance of it.

Regarding verification with asymptotic analytical solutions for hydraulic fracturing: The phase field approach has already been applied to hydraulic fracturing by multiple authors since 2012, see e.g., [6, 7, 8, 9, 10, 11, 12, 13]. Among these references, Wilson and Landis [15] and Chukwudzie [16] have already verified the phase field hydraulic fracture models with asymptotic solutions by Detournay and Garagash [17] and Hu and Garagash [18]. They verified the phase field model for both toughness-dominated and viscosity-dominated regimes, and found good agreement for pressure, aperture, and fracture length. At the beginning of Section 4, we now remind the readers of such existing verification results. As the phase field part of our method is based on the literature, and the main innovation is to model CO₂ fracturing by treating CO₂ as a compressible fluid, we did not plan to repeat such verifications for hydraulic fracturing.

The followings are a few comments:

1. The authors used a phase field depended permeability in their study. The permeability should be determined by the opening or close of fractures. Why could a damage variable be used to determine permeability? The phase field value is distributed over a range, however, a fracture creates jump in pressure and displacement. Why could a continuous variable be use to represent discontinuous behaviors, especially for permeability?

In smeared crack approaches such as the phase field method, the discontinuity is distributed over a finite width so that the sharp description of the crack is replaced by a diffusive description. This is precisely the key point of the variational theory of fracture, more commonly called the phase field approach, and its correctness was shown with the language of Γ -convergence, see, for example, Chambolle [19].

In this work, we have used the same idea for the permeability as well. See similar works [20, 21] with a damage model. In this regard, we have expanded the paragraph on p. 7 surrounding Equation (9) for more explanation.

2. Eq. 10 is not correct; which casts doubt on the whole sequentially coupled process. The treatment of porosity in Eq. 10 conflicts with the theory of poroelasticity. Change of porosity is not equal to the change of volumetric strain, not even in an approximate manner.

In [22], Verruijt proved that $\partial_t \varepsilon_v = (1 - \phi)\partial_t \phi$, assuming the grains are incompressible. On the other hand, Terzaghi [23] and Sheng *et al.* [24] suggested $\partial_t \varepsilon_v = \partial_t \phi$. In any case, as the porosity is relatively small ($\phi = 0.01$) we can still approximate the change of pore volume to that of the volumetric strain with minimal error. It is also worth mentioning that according to Wang *et al.* [1], the effect of the whole term $\rho\partial_t \phi$ is small compared with other terms.

3. Could the authors give the spatial and temporal discretization in appendix? Since the weak form is given already, spatial discretization is only one step away. I doubt the spatial discretization for a poroelastic medium could be derived from Eq. B1b or Eq. B2b. Though it is possible that the poroelastic model is ready for use in FEniCS package, the authors are suggested to provide the completely discretized formulations for the benefit of readers.

Following the reviewer's comment, now we have added the spatial and temporal discretizations to the current Appendix A. It is true that in our implementation, FEniCS itself computes this step.

4. Fully coupled examples are needed to verify the model. Correctly verifying a tensile test and the pressurization of a fracture do not indicate the model can correctly simulate hydraulic fracturing or CO₂ fracturing. The verification about pressurizing a bore hole is not a good example to show poroelastic responses. Actually, no typical poroelastic responses are shown in the example. Mandel's problem is suggested.

We appreciate the reviewer's suggestion. However, Mandel's problem is based on the assumption that the fluid is incompressible, while our main contribution is to model CO₂ as a compressible flow. Moreover, both being models with incompressible fluids, Mandel's problem would somehow repeat the second verification example (now Section 4.2) where the porous flow is coupled with the porous medium's displacement. Based on these reasons, we would prefer not to carry out Mandel's problem for this manuscript.

5. Please briefly explain the AT1 and AT2 model.

We now explained more about the AT1 and AT2 models on p. 5, under Equation (2).

6. line 1-2 Page 1 Are you sure shale or mudstone is the most common sedimentary rock?

We removed this phrase from the text.

Comments from Reviewer #4

The authors have proposed a model for CO₂ flow and fracturing in shale media. The manuscript has a good order, but needs revision to satisfy publication quality.

Gas flow in shale is one of the most challenging topics and has been widely investigated. The authors have used a relatively simple model for calculation of gas flow and permeability in shale media. A good model will capture important phenomena like Knudsen Diffusion and adsorption effect in shale rock media. Please modify this part of your model by providing a more holistic and detailed explanation. Please refer to series of papers by Javadpour et al. Also see: Seyyed A. Hosseini et al. "Novel Analytical Core-Sample Analysis Indicates Higher Gas Content in Shale-Gas Reservoirs" SPE Journal 2015.

We appreciate the reviewer's positive comments. Regarding phenomena like Knudsen diffusion and adsorption effect, we must recognize that each model has its scale of applicability. The proposed model is applicable to the continuum scale, aiming at simulating complex fracture processes, including fracture initiation, propagation and merging. As this work represents the first of its kind, a relatively simple model is used for the calculation of gas flow and permeability in shale media. For example, we simply used Darcy's law in a viscous flow regime (common in conventional reservoirs), as our continuum approach cannot afford explicitly capturing microscale phenomena like Knudsen diffusion. However there is potential to adopt more sophisticated phenomena like slip flow regime in future works in a multiscale simulation framework. Now we commented in Section 2.2 the works mentioned by the reviewer and admitted to our readers on p. 7, l. 145–150 of the simplicity of the model we used for the flow transport.

- [1] J. Wang, D. Elsworth, Y. Wu, J. Liu, W. Zhu, Y. Liu, The influence of fracturing fluids on fracturing processes: A comparison between water, oil and SC-CO₂, *Rock Mechanics and Rock Engineering* 51 (1) (2018) 299–313.
- [2] E. Eseme, J. L. Urai, B. M. Krooss, R. Littke, Review of mechanical properties of oil shales: Implications for exploitation and basin modelling, *Oil Shale* 24 (2).
- [3] C. Miehe, M. Hofacker, F. Welschinger, A phase field model for rate-independent crack propagation: Robust algorithmic implementation based on operator splits, *Computer Methods in Applied Mechanics and Engineering* 199 (45-48) (2010) 2765–2778.
- [4] E. Detournay, A.-D. Cheng, Poroelastic response of a borehole in a non-hydrostatic stress field, in: *International Journal of Rock Mechanics and Mining Sciences & Geomechanics Abstracts*, Vol. 25, Elsevier, 1988, pp. 171–182.
- [5] I. N. Sneddon, M. Lowengrub, *Crack Problems in the Classical Theory of Elasticity*, Wiley, New York, 1969.
- [6] B. Bourdin, C. P. Chukwudzie, K. Yoshioka, A variational approach to the numerical simulation of hydraulic fracturing, in: *SPE Annual Technical Conference and Exhibition*, Society of Petroleum Engineers, 2012, pp. SPE-159154-MS.
- [7] A. Mikelić, M. F. Wheeler, T. Wick, Phase-field modeling of pressurized fractures in a poroelastic medium, *ICES Report* (2014) 14–18.
- [8] K. Yoshioka, B. Bourdin, A variational hydraulic fracturing model coupled to a reservoir simulator, *International Journal of Rock Mechanics and Mining Sciences* 88 (2016) 137–150.

- [9] T. Wick, G. Singh, M. F. Wheeler, Fluid-filled fracture propagation with a phase-field approach and coupling to a reservoir simulator, *SPE Journal* 21 (03) (2016) 981–999.
- [10] S. Mauthe, C. Miehe, Hydraulic fracture in poro-hydro-elastic media, *Mechanics Research Communications* 80 (2017) 69–83.
- [11] W. Ehlers, C. Luo, A phase-field approach embedded in the theory of porous media for the description of dynamic hydraulic fracturing, *Computer Methods in Applied Mechanics and Engineering* 315 (2017) 348–368.
- [12] D. Culp, M. R. Tupek, P. Newell, M. H. Hubler, Phase-field modeling of fracture in CO₂ sequestration, in: 51st US Rock Mechanics/Geomechanics Symposium, American Rock Mechanics Association, 2017, pp. ARMA-2017-0644.
- [13] Y. Heider, B. Markert, Modelling of hydraulic fracturing and fluid flow change in saturated porous domains, *Proc. Appl. Math. Mech.* 17 (1) (2017) 95–98.
- [14] R. Span, W. Wagner, A new equation of state for carbon dioxide covering the fluid region from the triple-point temperature to 1100 K at pressures up to 800 MPa, *Journal of Physical and Chemical Reference Data* 25 (6) (1996) 1509–1596.
- [15] Z. A. Wilson, C. M. Landis, Phase-field modeling of hydraulic fracture, *Journal of the Mechanics and Physics of Solids* 96 (2016) 264–290.
- [16] C. Chukwudzie, Application of the variational fracture model to hydraulic fracturing in poroelastic media, Ph.D. thesis, Louisiana State University (2016).
- [17] E. Detournay, D. Garagash, The near-tip region of a fluid-driven fracture propagating in a permeable elastic solid, *Journal of Fluid Mechanics* 494 (2003) 1–32.
- [18] J. Hu, D. Garagash, Plane-strain propagation of a fluid-driven crack in a permeable rock with fracture toughness, *Journal of Engineering Mechanics* 136 (9) (2010) 1152–1166.
- [19] A. Chambolle, An approximation result for special functions with bounded deformation, *Journal de Mathématiques Pures et Appliquées* 83 (7) (2004) 929 – 954.
- [20] U. Pillai, Y. Heider, B. Markert, A diffusive dynamic brittle fracture model for heterogeneous solids and porous materials with implementation using a user-element subroutine, *Computational Materials Science* 153 (2018) 36 – 47.

- [21] W. Zhu, C. Wei, S. Li, J. Wei, M. Zhang, Numerical modeling on destress blasting in coal seam for enhancing gas drainage, International Journal of Rock Mechanics and Mining Sciences 59 (2013) 179 – 190.
- [22] A. Verruijt, Theory and Problems of Poroelasticity, 2013.
- [23] K. Terzaghi, Theoretical Soil Mechanics, John Wiley & Sons, New York, 1943.
- [24] M. Sheng, G. Li, S. N. Shah, X. Jin, Extended finite element modeling of multi-scale flow in fractured shale gas reservoirs, in: SPE Annual Technical Conference and Exhibition, Society of Petroleum Engineers, 2012, pp. SPE-159919-MS.

*Highlights (for review)

- We propose a phase field model to simulate CO₂ fracturing, where we solve a coupled system consisting of: (i) mass balance with modified Darcy's equation, and (ii) a dissipative potential energy with the phase field.
- CO₂ is treated as a compressible fluid under an isothermal condition in a porous medium by using the Span-Wagner equation of state.
- The implementation is verified through three examples. The predicted breakdown pressure agrees well with analytical solutions and, within 30%, with experiments.

1
2
3
4
5
6
7
8
9
10
11
12
13
14
15
16
17
18
19
20
21
22
23
24
25
26
27
28
29
30
31
32
33
34
35
36
37
38
39
40
41
42
43
44
45
46
47
48
49
50
51
52
53
54
55
56
57
58
59
60
61
62
63
64
65

Numerical modeling of CO₂ fracturing by the phase field approach

Mostafa Mollaali^a, Vahid Ziae-Rad^b, Yongxing Shen^{a,*}

^a*University of Michigan – Shanghai Jiao Tong University Joint Institute, Shanghai Jiao Tong University, Shanghai, China*

^b*Faculty of Civil, Water and Environmental Engineering, Shahid Beheshti University, Tehran, Iran*

Abstract

We propose a phase field model to simulate CO₂ fracturing under an isothermal condition. We take advantage of the ability of the phase field approach in predicting fracture initiation and branching, and also to avoid tracking the fracture path. We model the CO₂ as a compressible fluid by modifying Darcy's law. In particular, we assume the permeability is correlated to the phase field value by an exponential function. The dependence of the CO₂ density as a function of the pressure is captured by the Span-Wagner equation of state. The computed breakdown pressure values show good agreement with analytical solutions and experimental results.

Keywords: CO₂ fracturing, CO₂ fluid flow, phase field

2010 MSC: 65K10

1. Introduction

Shale gas is the natural gas trapped within the shale, or mudstone reservoir,⁵ the most common sedimentary rock. Shale is a fine-grained, sedimentary rock composed of clay minerals and silt-sized particles. The shale has low permeability so that it significantly inhibits the gas flow from the reservoir rocks to the production wells. As a result, the economic feasibility of shale gas development relies on the effective stimulation of the reservoirs [1]. Shale gas has become an energy source of increasing worldwide interest due to the two technologies that have become mature in industry: horizontal drilling and hydraulic fracturing technique [2].

To date, water-based fluids are the most important fluids regularly used in the commercial shale gas due to their ready availability and low cost. But there are also some disadvantages to use water-based fluids, namely water shortage, contamination of underground water, and low fracturing performance. Also,

*Corresponding author
Email address: yongxing.shen@sjtu.edu.cn (Yongxing Shen)

1
2
3
4
5
6
7
8
9 15 hydraulic fracturing cannot avoid the clay swelling problem in shale [2]. Due
10 to these problems, researchers actively investigate non-aqueous (see [3]) and
11 non-fluid fracturing techniques such as explosive based method [4].

12 16 Carbon dioxide (CO_2) is one of the non-aqueous fracturing fluids that is
13 considered to be used for fracturing. CO_2 as a fracturing fluid has been success-
14 20 fully applied to fracturing unconventional gas reservoirs decades ago [5]. Since
15 the critical temperature of CO_2 is 31.1°C , once the pressure exceeds its critical
16 pressure of 7.38 MPa, it will change to the supercritical state [6]. It can be
17 injected down-hole either in liquid or supercritical state. The main benefits of
18 CO_2 as a fracturing fluid include reducing consumption of water and water con-
19 tamination, keeping clays (smectite and illite) stabilized, and preventing metal
20 leaching and chemical interactions.

21 22 Brown [7] proposed CO_2 as a fracturing fluid and circulating fluid in geother-
23 mal energy extraction. Middleton *et al.* [8] investigated the potential of using
24 CO_2 as a fracturing fluid for commercial scale of shale production. In the lab-
25 30 oratory scale, Ishida *et al.* [9, 10] conducted fracturing experiments by using
26 supercritical CO_2 . Also, some researchers investigated the effect of different
27 fracturing fluids [11, 12].

28 29 There exist two general approaches for modeling fracture. One is discrete
30 models for fracture where the geometrical discontinuity is modeled by modi-
31 35 fying the geometry of intact structure [13, 14, 15, 16]. The other is smeared
32 crack models where the discontinuity is distributed over a finite width, such as
33 the phase field [17] and the gradient-enhanced damage methods [18]. In this
34 approach, an additional unknown and a length scale are introduced.

35 36 Phase field modeling of fracture has gained popularity since the beginning of
37 this century. The phase field model by Bourdin *et al.* [17] is essentially a regulariza-
38 40 tion of the variational formulation of brittle fracture by Francfort and Marigo
39 [19]. What makes the phase field an attractive approach can be attributed to
40 45 its convenience in simulating complex fracture processes, including crack ini-
41 tiation, propagation, branching and merging. Compared to discrete fracture
42 descriptions, the phase field approaches avoid tracking the complicated crack
43 geometry; instead, the crack evolution is a natural outcome of the numerical
44 solution to a constrained optimization problem. Thus, it significantly decreases
45 the implementation difficulty, especially when dealing with 3D problems.

46 47 Bourdin *et al.* [20] have adopted the phase field approach to model hydraulic
48 fracturing in impermeable media by considering the force that fluid pressure
49 exerts on fracture surfaces. Afterwards, phase field approaches for hydraulic
50 55 fracture in porous media based on Biot's equations and the theory of porous
51 media have been investigated by many researchers.

52 53 Mikelić *et al.* [21] model pressurized fracture in porous media by combining
54 the Biot theory and phase field approach. To minimize code modifications for
55 adopting the phase field approach with an existing reservoir simulator, Yoshioka
56 and Bourdin [22] have proposed an efficient framework by modifying the Darcy
57 law. Wick *et al.* [23] have developed a model to simulate fluid-filled fracture
58 propagation coupled to a reservoir simulator. Also, they have used a single
59 pressure equation for the entire fractured domain by introducing a function to

1
2
3
4
5
6
7
8
9
10
11
12
13
14
15
16
17
18
19
20
21
22
23
24
25
26
27
28
29
30
31
32
33
34
35
36
37
38
39
40
41
42
43
44
45
46
47
48
49
50
51
52
53
54
55
56
57
58
59
60
61
62
63
64
65

distinguish between reservoir and fracture domains. Mauthe and Miehe [24] have coupled the phase field hydraulic fracture and porous media fluid flow by using a permeability decomposition. Ehlers and Luo [25] have combined the theory of porous media (TPM) and the phase field approach to fracture. Also, Culp *et al.* [26] have applied the phase field approach to fracture in CO₂ sequestration. In most cases researchers have supposed the fracturing fluid is incompressible or slightly compressible. Recently, Heider and Markert [27] proposed a method to model the pore fluid which is considered compressible.

The objective of the paper at hand is to propose a phase field model to investigate the effect of CO₂ as a compressible fracturing fluid under the isothermal condition, as the first step towards such modeling. For this purpose, we have adopted the phase field approach to model fracturing in porous media according to Mikelić *et al.* [21]. We model the CO₂ flow as a compressible fluid by modifying Darcy's law. We suppose permeability is correlated to the phase field value by an exponential function. The CO₂ density varies significantly with pressure, which is captured by the Span-Wagner equation of state [28].

In the remaining paper we will proceed as follows: a description of the fracture problem is given in Section 2, including the governing equations of the solid and the fluid flow. Afterwards, the numerical discretization and algorithm are constructed in Section 3. Then Section 4 provides numerical examples and discussions, where we will show that our results for the breakdown pressure agree well with not only widely used analytical solutions but also, within a reasonable error, with experimental results. Finally Section 5 draws conclusions.

2. Mathematical model

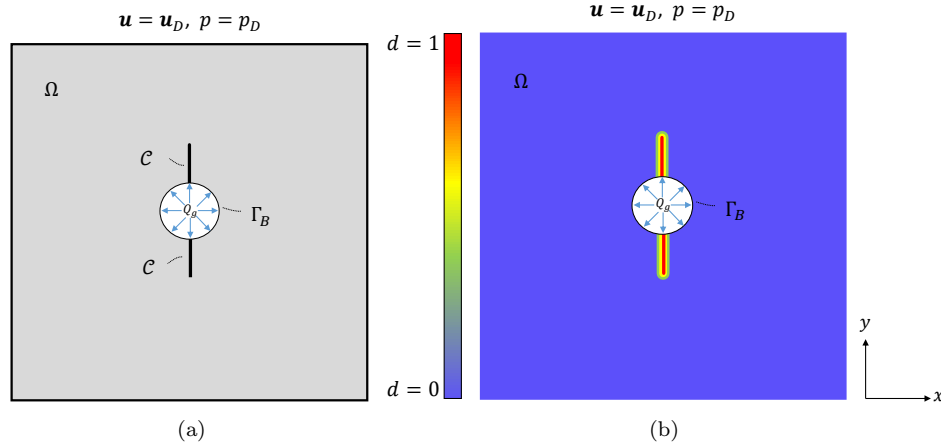
This section describes the mathematical model we will adopt for CO₂ fracturing. For convenience we will confine ourselves to the two-dimensional plane strain case, but the formulation is applicable to three dimensions with minimal changes. During the CO₂ fracturing process, the gas penetrates into the rock around the borehole and the injecting pressure causes the fracture to propagate. Thus, fracture propagation is a coupled phenomenon involving the gas flow inside the fracture and in the entire porous medium, the rock deformation, and the fracture propagation in the rock mass. In the following, in Section 2.1 we introduce the phase field method for fracture and derive the governing equations for the deformation and fracture propagation in the porous medium. Then, in Section 2.2 we present the governing equations for the gas flow within the porous medium. It is worth mentioning that compressible CO₂ exhibits a transport behavior different from that of slightly compressible fluids such as water and oil, due to its large compressibility and possibility of phase change.

2.1. Porous medium deformation and fracture propagation

In this section, we briefly recapitulate the basic notations and the underlying equations of the phase field method for pressurized fractures in brittle materials.

1
2
3
4
5
6
7
8
9 **2.1.1. Variational formulation of brittle fracture**

10 We consider a two-dimensional porous medium under plane strain loading
 11 occupying an open Lipschitz domain $\Omega \subset \mathbb{R}^2$. Let $\Gamma_D, \Gamma_N \subseteq \partial\Omega$ be such that
 12 $\Gamma_D \cup \Gamma_N = \partial\Omega$ and $\Gamma_D \cap \Gamma_N = \emptyset$, and $\mathbf{u}_D : \Gamma_D \rightarrow \mathbb{R}^2$ and $\mathbf{t}_N : \Gamma_N \rightarrow \mathbb{R}^2$ be
 13 prescribed displacement and traction boundary conditions, respectively. Also,
 14 let $\Gamma_B \subset \partial\Omega$ denote the boundary of a borehole. We let $Q_g : \Gamma_B \rightarrow \mathbb{R}$ denote
 15 the fluid source and $\mathbf{b} : \Omega \rightarrow \mathbb{R}^2$ the body force per unit volume exerted to the
 16 solid.
 17



34 Figure 1: Schematic of (a) a sharp fracture and (b) the diffusive phase field profile for the
 35 in both figures, a square plate with a borehole placed inside is shown. The *in*
 36 *situ* stress is applied on the external boundary, while the fluid is injected from the boundary
 37 of the borehole. **We will only use the diffusive phase field in the proposed method.**

38 The variational approach to fracture is built on energy minimization with
 39 respect to the displacement field $\mathbf{u} : \Omega \rightarrow \mathbb{R}^2$ and its jump set, which we denote
 40 as $\mathcal{C} = \mathcal{C}(\mathbf{u}) \subset \Omega$. Let $|\mathcal{C}|$ denote the one-dimensional Hausdorff measure of \mathcal{C} .
 41 Following Griffith's theory, the total potential energy of the fractured poroelastic
 42 solid is written as:
 43

$$\begin{aligned} \Pi_{\mathcal{C}}[\mathbf{u}, \mathcal{C}] := & \int_{\Omega \setminus \mathcal{C}} \psi_0[\varepsilon(\mathbf{u})] d\Omega - \int_{\Omega} \mathbf{b} \cdot \mathbf{u} d\Omega - \int_{\Gamma_N} \mathbf{t}_N \cdot \mathbf{u} d\Gamma \\ & - \int_{\Omega \setminus \mathcal{C}} (\alpha - 1) p \operatorname{div} \mathbf{u} d\Omega + \int_{\Omega \setminus \mathcal{C}} \nabla p \cdot \mathbf{u} d\Omega + g_c |\mathcal{C}|, \end{aligned} \quad (1)$$

49 where p denotes the pore pressure, $\alpha \in [0, 1]$ is the Biot coefficient. Constant
 50 $g_c \in \mathbb{R}^+$ is the strain energy released per unit length of fracture extension. The
 51 strain energy density $\psi_0[\varepsilon(\mathbf{u})]$ is given by
 52

$$\psi_0(\varepsilon) := \frac{\lambda}{2} (\operatorname{tr} \varepsilon)^2 + G \|\varepsilon\|^2,$$

55 with λ and G Lamé constants. These constants are related to Young's modulus
 56 E and Poisson's ratio ν as $\lambda = E\nu / [(1+\nu)(1-2\nu)]$ and $G = E / [2(1+\nu)]$. The
 57
 58

linearized strain tensor takes the form:

$$\boldsymbol{\varepsilon}(\mathbf{u}) := \frac{1}{2} (\nabla \mathbf{u} + \nabla \mathbf{u}^T).$$

Finally, $\|\cdot\|$ denotes the Frobenius norm of a tensor.

2.1.2. Regularized variational formulation of brittle fracture

To develop a numerical method to approximate (1), the phase field approach replaces the sharp-fracture description \mathcal{C} with a phase field description, where the phase field is denoted as $d : \Omega \rightarrow [0, 1]$. In particular, regions with $d = 0$ and $d = 1$ correspond to the intact and fully broken materials, respectively. Using a phase field approach, the one-dimensional fracture \mathcal{C} is approximated with the help of an elliptic functional [29, 30]:

$$\mathcal{C}_\ell[d] := \frac{1}{4c_w} \int_{\Omega} \left(\frac{w(d)}{\ell} + \ell \nabla d \cdot \nabla d \right) d\Omega, \quad (2)$$

where $\ell > 0$ is the regularization length scale, which may also be interpreted as a material property, e.g., the size of the process zone. See Remark 3 for comments on the choice of ℓ . Constant $c_w = \int_0^1 \sqrt{w(d)}$ is a normalization constant such that when $\ell \rightarrow 0$, $\mathcal{C}_\ell[d]$ converges to the length of the sharp fracture, $|\mathcal{C}|$. Classical examples of $w(d)$ and c_w are $w(d) = d^2$ and $c_w = 1/2$ for the AT2 model, and $w(d) = d$ and $c_w = 2/3$ for the AT1 model. Between these models, the AT1 model which is better at simulating crack nucleation [31] predicts a phase field profile with a support of a finite width, but requires solving inequality constrained optimization problems; the AT2 model, which normally requires a pre-existing crack (at least for a homogeneous material under low-speed loading), gives a diffuse phase field profile, but can be implemented as constrained optimization problems which are much easier to solve. Interested readers are referred to [31, 32] for more elaborations. In this paper all numerical examples are implemented with the AT1 model, while we keep our formulation general for both models.

On this basis, we replace (1) by a global constitutive dissipation functional for a rate independent fracture process [33]:

$$\begin{aligned} \Pi[\mathbf{u}, d] := & \int_{\Omega} \psi[\boldsymbol{\varepsilon}(\mathbf{u}), d] d\Omega - \int_{\Omega} \mathbf{b} \cdot \mathbf{u} d\Omega - \int_{\Gamma_N} \mathbf{t}_N \cdot \mathbf{u} d\Gamma \\ & - \int_{\Omega} (1-d)^2 (\alpha - 1) p \operatorname{div} \mathbf{u} d\Omega + \int_{\Omega} (1-d)^2 \nabla p \cdot \mathbf{u} d\Omega \\ & + \frac{g_c}{4c_w} \int_{\Omega} \left(\frac{w(d)}{\ell} + \ell \nabla d \cdot \nabla d \right) d\Omega, \end{aligned} \quad (3)$$

where the admissible sets of displacement and phase field can be set as:

$$\mathcal{S}_u := \{ \mathbf{u} \in H^1(\Omega; \mathbb{R}^2) | \mathbf{u} = \mathbf{u}_D \text{ on } \Gamma_D \}, \quad (4a)$$

$$\mathcal{S}_d := \{ d \in H^1(\Omega) | 0 \leq d \leq 1 \}. \quad (4b)$$

In practice, (4b) will be used in combination with the irreversibility constraint, to be elaborated in Remark 2.

Remark 1 (Strain energy degradation). *The solid endures partial loss of stiffness due to the presence of fractures. In order to model this effect, the strain energy density is degraded with respect to the evolution of the phase field. Also note that as the damaged material responds differently to tension and compression, we let only a part of the strain energy density be degraded. For this purpose, we let the degraded strain energy in (3) take the following general form:*

$$\psi(\boldsymbol{\varepsilon}, d) = g(d)\psi_+ + \psi_-,$$

where $g(d)$ satisfies $g(0) = 1$, $g(1) = 0$, and $g'(d) < 0$ for all d such that $0 \leq d \leq 1$ [17]. A usual choice is $g(d) = (1 - d)^2$. On the other hand, ψ_{\pm} are such that

$$\psi_+(\boldsymbol{\varepsilon}) + \psi_-(\boldsymbol{\varepsilon}) = \psi_0(\boldsymbol{\varepsilon}).$$

Now since $\partial\psi/\partial d = g'(d)\psi_+$, only ψ_+ contributes to fracture propagation.

There are several phase field models that differ in their choice of ψ_{\pm} . In this paper, we adopt the one proposed by Amor *et al.* [34]. This model assumes both volumetric expansion and deviatoric deformation contribute to fracture propagation, but volumetric compression does not. A decomposition of $\boldsymbol{\varepsilon}$ into volumetric and deviatoric parts reads:

$$\text{vol } \boldsymbol{\varepsilon} := \frac{1}{3}(\text{tr } \boldsymbol{\varepsilon})\mathbf{1}, \quad \text{dev } \boldsymbol{\varepsilon} := \boldsymbol{\varepsilon} - \text{vol } \boldsymbol{\varepsilon}.$$

See AppendixA.1 for more details.

Remark 2 (Irreversibility constraint). *The requirement $g'(d) < 0$ comes from the underlying irreversibility condition (the fracture can never heal) in time:*

$$\partial_t d \geq 0. \tag{5}$$

Consequently, modeling of fracture evolution problems leads to inequality constraints, and sometimes gives rise to a variational inequality formulation.

As an alternative way to model the irreversibility, Miehe *et al.* [35] proposed a phase field model based on a local history field. In this model, the evolution of the phase field d is driven by the historically maximum value of ψ_+ at the point of interest.

Remark 3 (The choice of ℓ). *Based on an analytical solution for the critical tensile strength σ_{cr} that a one-dimensional bar can sustain [32], we use the following equation for the choice of ℓ :*

$$\ell = \frac{3Eg_c}{8\sigma_{cr}^2}, \tag{6}$$

where E and g_c can be obtained from regular experiments, while σ_{cr} can be approximated by the tensile strength σ_t . Assuming all other parameters are known, the formula (6) is able to estimate ℓ , though the accuracy is unknown for more complex cases.

1
2
3
4
5
6
7
8
9 *2.2. Carbon dioxide as a compressible fluid*

10 The governing equations for the fluid flow in a porous medium are given by
11 mass conservation, momentum balance, and the equation of state. The mass
12 conservation equation reads:

$$\begin{aligned} \partial_t(\phi\rho) + \nabla \cdot (\rho\mathbf{v}) &= 0 && \text{in } \Omega, \\ -\rho\mathbf{v} \cdot \mathbf{n} &= Q_g && \text{on } \Gamma_B. \end{aligned} \quad (7)$$

17 Here ϕ denotes the porosity of the porous medium (the fraction of volume
18 occupied by the fluid), ρ the density of the fluid, \mathbf{v} the Darcy velocity vector,
19 and Q_g the fluid source. Note that Q_g has the unit of volumetric flow rate per
20 unit volume. Also, we assume the rock is saturated by the fluid so that the fluid
21 content in rock per volume is expressed by $\phi\rho$.
22

23 In addition to (7), we state the momentum balance in the form of Darcy's
24 law. Note that this assumption is for the flow in conventional reservoirs, al-
25 though there are more complicated flow regimes, namely slip flow, transition
26 flow, and Knudsen diffusion, for which Darcy's law in its current form cannot
27 be used. For more details we refer the reader to [36, 37, 38, 39]. Nevertheless
28 modeling the flow at the microscale is out of the scope of this paper that
29 deals with a continuum formulation, and hence we confine ourselves to Darcy's
30 law throughout this work. This implies a linear relationship between the fluid
31 velocity and the head pressure gradient:
32

$$\mathbf{v} = -\frac{k}{\mu} \nabla p, \quad (8)$$

33 where $k = k(d)$ is the permeability of the rock, and μ is the dynamic fluid
34 viscosity. Note that there could be an additional term $-\rho g \nabla z$ on the right hand
35 side of (8), where g and z are the magnitude of the gravitational acceleration
36 and the depth, respectively. This term is, however, in our case negligible, as
37 we assume an almost horizontal computational domain. Also, we assume the
38 porosity is not dependent on the stress condition.
39

40 On the other hand, we correlate the permeability to the phase field value
41 as it is clear that when the crack starts propagating, the permeability of the
42 solid matrix starts to increase, as the crack width increases. To incorporate
43 this effect into our model, an exponential variation of the fluid permeability has
44 been adopted from [40, 41]:
45

$$k(d) = k_0 \exp(\alpha_k d), \quad (9)$$

46 where k_0 is the permeability of the intact material, and α_k is a coefficient to
47 indicate the effect of phase field evolution on the permeability. We take $\alpha_k = 7.0$
48 according to [41]. In real applications, α_k can be obtained from experiments.
49 Figure 2 illustrates the permeability increasing with respect to the evolution of
50 the phase field variable. As seen therein, the permeability starts from an initial
51 value for a completely intact porous medium to a very big value of permeability
52 in the fully broken area.
53

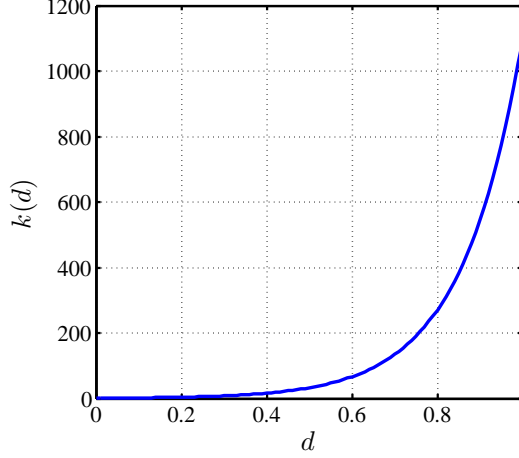


Figure 2: Plot of $k(d) = \exp(7.0d)$, permeability, as a function of the phase field variable d .

The first term on the left hand side of (7), the rate of change of fluid content, can be written as:

$$\partial_t (\phi\rho) = \rho \partial_t \phi + \phi \partial_t \rho = \rho \partial_t \varepsilon_v + \phi \partial_t \rho, \quad (10)$$

where we have assumed the rate of change of pore volume is equal to that of the volumetric strain, which is given by $\varepsilon_v = \nabla \cdot \mathbf{u}$.

Under isothermal conditions, the gas density varies significantly with pressure. This is captured by an equation of state (EOS). One applicable EOS for CO₂ is known as the Span-Wagner (S-W) equation [28] defined in terms of the Helmholtz free energy. The CO₂ density and pressure are related by:

$$p = (1 + \delta\varphi_\delta^r) \rho RT, \quad (11)$$

where R is the universal gas constant, and φ_δ^r is the derivative of the residual part of the full expression of Helmholtz energy φ^r with respect to the reduced density δ , with

$$\begin{aligned} \varphi^r(\delta, \tau) = & \sum_{i=1}^7 n_i \delta^{d_i} \tau^{t_i} + \sum_{i=8}^{34} n_i \delta^{d_i} \tau^{t_i} e^{-\delta^{c_i}} + \sum_{i=35}^{39} n_i \delta^{d_i} \tau^{t_i} e^{-\alpha_i(\delta - \varepsilon_i)^2 - \beta_i(\tau - \gamma_i)^2} \\ & + \sum_{i=40}^{42} n_i \Delta^{b_i} \delta e^{C_i(\delta - 1)^2 - D_i(\tau - 1)^2}, \end{aligned} \quad (12)$$

in which

$$\Delta = \left\{ (1 - \tau) + A_i \left[(\delta - 1)^2 \right] \frac{1}{2\beta_i} \right\}^2 + B_i \left[(\delta - 1)^2 \right]^{a_i}.$$

In (12), ρ_c and T_c are the critical density and temperature, respectively, and $\delta = \rho/\rho_c$ and $\tau = T/T_c$ are the reduced ones. For the sake of brevity, here we do not provide the definitions and values of other parameters in (12), but refer the readers to [28].

By substituting (8),(9), (10), and (11) in (7), the governing equation for CO₂ flow is written as follows:

$$\begin{aligned} \phi \partial_t \rho + \rho \partial_t \varepsilon_v - \nabla \cdot \left(\rho \frac{k(d)}{\mu} \nabla p \right) &= 0, \quad \text{in } \Omega, \\ \rho \mathbf{v} \cdot \mathbf{n} &= -Q_g, \quad \text{on } \Gamma_B, \\ p &= p_D, \quad \text{on } \Gamma_P, \end{aligned} \tag{13}$$

where $\Gamma_P = \partial\Omega \setminus \Gamma_B$.

Summary of governing equations. The governing equations for modeling the CO₂ fracturing are summarized as follow: for the porous medium deformation, the functional defined in (3) is minimized among $(\mathbf{u}, d) \in \mathcal{S}_u \times \mathcal{S}_d$ under the constraint (5), while for the compressible fluid the boundary value problem (13) is used to solve for the pressure p .

Advantages and limitations of the method. The main advantage of the current approach is its convenience in simulating complex fracture processes, including crack initiation, propagation and merging. In fact, the evolution of fracture surfaces is the natural outcome of the solution of a coupled system of partial differential equations. Such a model significantly decreases the implementation difficulty by avoiding tracking the fracture geometry. In this work, taking advantage of the phase field approach, we consider CO₂ as a compressible fracturing fluid under an isothermal condition. Nevertheless, as this work is the first of its kind, herein a relatively simple model is used for the calculation of gas flow and permeability in shale media.

3. Numerical solution

In this section we present an algorithm that adopts standard procedures to obtain a numerical method to solve the initial boundary value problem presented in Section 2. In this algorithm, a staggered approach is employed to solve the underlying equations, i.e., the solution is obtained via iteration between the variables [17, 42]. This idea is based on the fact that by fixing two variables, the problem becomes convex in the remaining unknown. However, one drawback for such an approach is that it might need many iterations to achieve convergence among the three fields.

For the problem at hand, we need to solve a coupled system consisting of mass balance for the compressible fluid and a dissipative potential energy with the phase field. We provide a fully iterative approach in which at each stage we solve for one unknown while the other two variables are fixed to their values at the last iteration. Readers are referred to Algorithm 1 for complete elaboration.

Algorithm 1: Algorithm for modeling the CO₂ by phase field.

22 **Input:** $p_0, d_0, \mathbf{u}_0, \rho_0$, and ε_{tol}
23 **Output:** p_n, d_n , and $\mathbf{u}_n, n = 1, \dots, N$
24 1 Set flow and mechanical boundary conditions σ_1, σ_3 , and Q_g ;
25 2 **for** $n = 1$ to N ; **do**
26 3 Set $t = n\Delta t$ and $k = 0$; /* k is an iteration counter */
27 4 **repeat**
28 5 $m = 0$; /* m is another iteration counter */
29 6 **repeat**
30 7 Step - P: compute p_n with (A.6);
31 8 Step - U: compute \mathbf{u}_n with (A.1);
32 9 Update $\rho_n^{(k+1)} \leftarrow \rho(p_n^{(k)})$ with (11);
33 10 $k + 1 \leftarrow k$
34 11 **until** $\|p_n^{(k)} - p_n^{(k-1)}\|_2 < \varepsilon_{\text{tol}}$ and $\|\mathbf{u}_n^{(k)} - \mathbf{u}_n^{(k-1)}\|_2 < \varepsilon_{\text{tol}}$;
35 12 Step - d: compute d_n with (A.1);
36 13 $m + 1 \leftarrow m$
37 14 **until** $\varepsilon_d = \|d_n^{(m)} - d_n^{(m-1)}\|_2 < \varepsilon_{\text{tol}}$;
38 15 $\mathbf{u}_{n-1} \leftarrow \mathbf{u}_n$;
39 16 $p_{n-1} \leftarrow p_n$;
40 17 $\rho_{n-1} \leftarrow \rho_n$;
41 18 **end**

We implement our method on FEniCS, an open-source finite element software [43, pp. 173–225]. Therein, the user merely needs to provide the variational form of the problem as well as the geometry and mesh information. Then, a big advantage of FEniCS is that the software itself completes all steps toward generating the global stiffness matrix.

Below we show an excerpt of the used FEniCS code. This piece of code performs some calculations for line 8 in Algorithm 1 wherein \mathbf{u} is solved for while the other two unknowns are fixed. It first defines $\boldsymbol{\varepsilon}$, ψ_0 , and $\psi(\boldsymbol{\varepsilon}, d)$ in lines 1, 3, and 5, respectively. Then, the standard finite element shape functions are defined in line 8, and the admissible function space (`TrialFunction`), the test function space (`TestFunction`), and the unknown function \mathbf{u} (`Function`) are defined in line 9. Afterwards, the elastic energy is introduced as a variational form in line 11. Finally, in lines 12 and 13, the code takes the first variation $\delta\Pi[(\mathbf{u}, d); \bar{\mathbf{u}}]$ (A.1a) and the second variation $\delta^2\Pi[(\mathbf{u}, d); \bar{\mathbf{u}}; \delta\mathbf{u}]$ (A.2a) and builds the nodal residual vector as `Residual_u` and the tangent stiffness matrix as `Jacobian_u`.

```

1 def eps(u_):
2     return sym(grad(u_))
3 def psi_0(u_):
4     return 0.5 * lmbda * tr(eps(u_))**2 + mu * eps(u_)**2
5 def psi_(u_, d_):
6     return ((1 - d_)**2 + k_ell) * psi_0(u_)
7
8 V_u = VectorFunctionSpace(mesh, "CG", 1)
9 u_, u, u_t = Function(V_u), TrialFunction(V_u), TestFunction(V_u)
10
11 energy_elastic = psi_(u_, d_) * dx
12 Residual_u = derivative(energy_elastic, u, u_t)
13 Jacobian_u = derivative(Residual, u_, u_t)

```

To solve the three unknowns, we select for \mathbf{u} and p the linear solver MUMPS which is convenient for solving large linear systems [44], and for d the TAO optimization solver integrated into the PETSc library [45, 46], which has the capability of solving inequality constrained optimization problems as the one at hand. Interested readers are referred to [47] for more information about the applied solvers.

4. Numerical examples

In this section, we present a set of numerical examples to demonstrate the capability of the proposed model. First, we aim to verify our implementation of the present phase field method for CO₂ fracturing. To this end, we present three examples with exact or otherwise well-established solutions to verify our outputs. Next, we present three more numerical example to demonstrate the capability of the proposed model.

1
2
3
4
5
6
7
8
9
10
11
12
13
14
15
16
17
18
19
20
21
22
23
24
25
26
27
28
29
30
31
32
33
34
35
36
37
38
39
40
41
42
43
44
45
46
47
48
49
50
51
52
53
54
55
56
57
58
59
60
61
62
63
64
65

240 We also refer the interested readers to Wilson and Landis [48] and Chukwudzie [49] in which the phase field approach to hydraulic fracturing is verified
241 with classical two-dimensional analytical solutions [50, 51].

4.1. Single-edge-notched tension test

245 First, following an example motivated by Miehe *et al.* [52], we first investigate
246 a square plate with a horizontal initial crack at the middle height starting from
247 the left end and ending at the plate center. The geometric setup is depicted
248 in Figure 10. To capture the crack pattern properly, the mesh is refined in
249 areas where the crack is expected to propagate, i.e., in the center strip of the
250 specimen. In effect, for a discretization with 105,352 standard P_1 elements,
251 an effective element size of $h \approx 5 \times 10^{-3}$ mm is obtained in the critical zone.
252 The specimen is under a direct tension test, in which a monotonically increasing
253 displacement with constant increments $\Delta u = 6 \times 10^{-5}$ mm is imposed on the top
254 edge while the bottom edge is fixed. In this example, the evolution is simulated
255 for 100 uniform time steps so that a final deformation of 6×10^{-3} mm is reached.
We will adopt the values of the material parameters given in Table 1. Note that
all our models are implemented with the AT1 model.

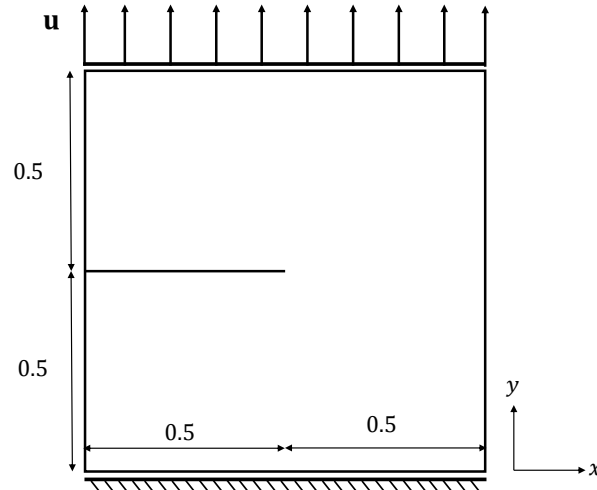


Figure 3: Schematic of a cracked square plate (unit: mm) under a single-edge-notched tension test. A monotonically increasing displacement with constant increments $\Delta u = 6 \times 10^{-5}$ mm is applied on the top edge while the bottom edge is fixed.

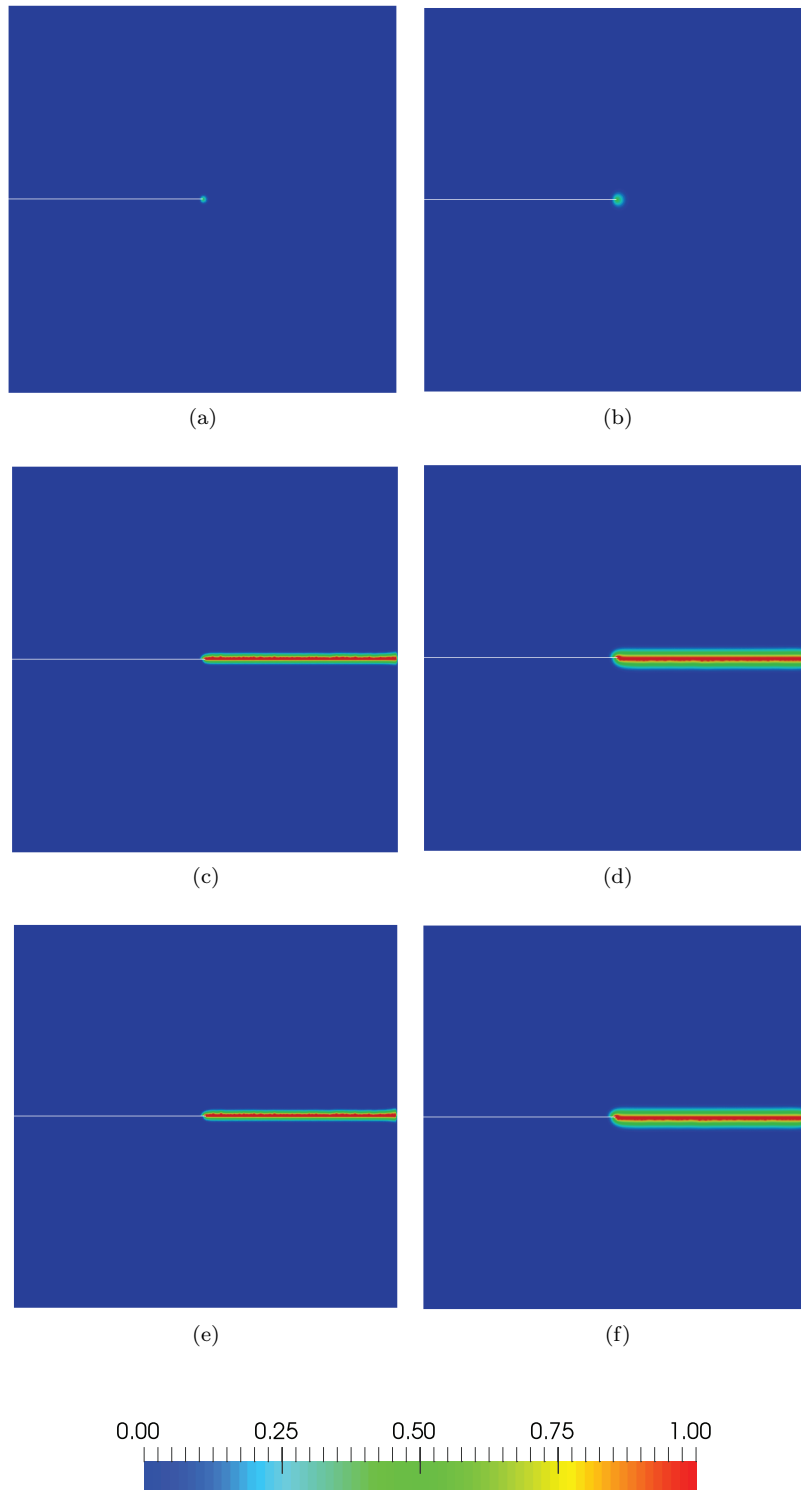
Table 1: Cracked square plate under a tension test: Material parameters [53]

| Parameters | symbol | unit | value |
|------------------------------|--------|--------|-------------------|
| Young's modulus | E | MPa | 210×10^3 |
| Poisson's ratio | ν | — | 0.3 |
| Critical energy release rate | g_c | MPa·mm | 2.7 |

The resulting crack patterns at different stages of the deformation for two fixed regularization length scales $\ell = \ell_1 = 1 \times 10^{-2}$ mm and $\ell = \ell_2 = 2 \times 10^{-2}$ mm are illustrated in Figure 4. As expected, in both simulations, the fracture propagates straightforward to the end. This straight crack topology agrees well with the results in [54]. Also as seen, the resulting crack pattern with the smaller ℓ looks sharper.

We also output the load-deflection curves for the two setups of Figure 5. As seen, both models will result in similar trends. Hence, the effect of ℓ on the response is small in this range.

1
2
3
4
5
6
7
8
9
10
11
12
13
14
15
16
17
18
19
20
21
22
23
24
25
26
27
28
29
30
31
32
33
34
35
36
37
38
39
40
41
42
43
44
45
46
47
48
49
50
51
52
53
54
55
56
57
58
59
60
61
62
63
64
65



14

Figure 4: Cracked square plate under a tension test with two different regularization length scales $\ell = \ell_1 = 10^{-2}$ mm $\approx 2h$ (left) and $\ell = \ell_2 = 2 \times 10^{-2}$ mm $\approx 4h$ (right). Both simulations are done with 100 uniform time steps with $\Delta u = 6 \times 10^{-5}$ mm (See also Table 1 for the input values). Phase field contours at three different stages $u = 5.52 \times 10^{-3}$ mm (4a,4b), $u = 5.58 \times 10^{-3}$ mm (4c,4d), and $u = 6 \times 10^{-3}$ mm (4e,4f) are shown in deformed configurations with the deformations scaled. The initial cracks are explicitly imposed, so in the deformed configuration it appears as a white line. As expected, we observe a straight crack pattern in both cases.

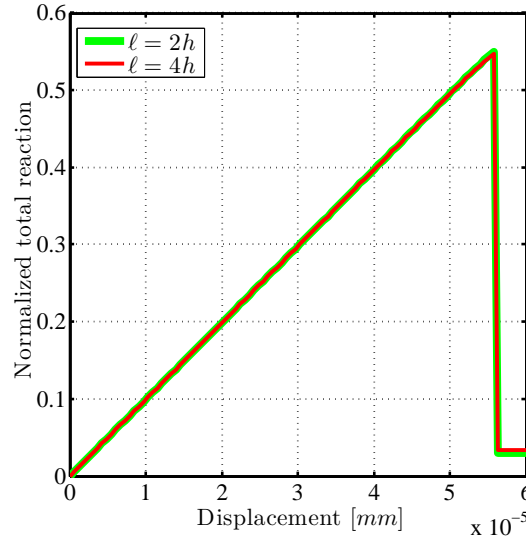


Figure 5: Cracked square plate under a tension test with two different regularization length scales $\ell = \ell_1 = 10^{-2}$ mm $\approx 2h$ (red) and $\ell = \ell_2 = 2 \times 10^{-2}$ mm $\approx 4h$ (green). Load-deflection curves for both ℓ_1 and ℓ_2 are obtained. Both simulations are done with 100 load steps with $\Delta u = 6 \times 10^{-5}$ mm. The total reaction is normalized by the one in the case without any crack or phase field evolution. Both models give rise to similar trends so the effect of changes in ℓ is small within this range. Note that the reaction highly decreases at the 93rd time step where the crack starts to propagate.

1
2
3
4
5
6
7
8
9 4.2. Poroelastic response of a borehole

10 This example aims to study the effect of fluid pressurization on the poroelastic
 11 response around the borehole. It was first studied by Detourneau and Cheng
 12 [55] (see also [11, 56]). Consider a plane strain hydraulic fracturing problem
 13 where there is a square plate containing a central borehole. The geometry and
 14 the loading conditions in this example are the same as Figure 12. The far-field
 15 *in situ* stress is set to zero in this example. Note also that $d \equiv 0$, i.e., there is
 16 no preexisting crack in the specimen and we do not allow for any nucleation of
 17 the fracture as the rock strength is assigned a very large value. A discretization
 18 with 28,140 standard P_1 elements is applied to the problem. To capture the
 19 high gradient of pressure near the borehole, the mesh is refined in that area so
 20 that an effective mesh size of $h \approx 0.15$ mm is adopted. The fluid is slightly
 21 compressible, and we set the fluid pressure in the borehole to 1 MPa. The other
 22 material properties are prescribed according to Table 2.

23 Here, the governing equation for the slightly compressible flow is written as
 24 follows [55]:
 25

$$\partial_t p + M \nabla \cdot \left(\frac{k_0}{\mu} \nabla p \right) = 0$$

26 where $M = E(1-\nu)/[(1+\nu)(1-2\nu)]$ is called the constrained modulus.
 27
 28

30 Table 2: Poroelastic response of a borehole: Material parameters
 31

| Parameters | symbol | unit | value |
|------------------|----------|-----------------|---------------------|
| Young's modulus | E | MPa | 6000 |
| Poisson's ratio | ν | — | 0.34 |
| Biot coefficient | α | — | 1. |
| Permeability | k_0 | mm ² | 1×10^{-12} |

32 Figure 6 shows the distribution of pore pressure around the borehole for three
 33 values of dynamic viscosity μ at early time $t = 0.1$ s. Note that the horizontal
 34 axis is $(r - r_0)/r_0$, ranging from 0 to 0.25 in the direction of $\theta = \pi/2$. The
 35 simulation results are then compared to the analytical solution by Detourneau
 36 and Cheng [55].
 37

38 Figure 7 depicts the effect of dynamic viscosity on the effective tangential
 39 stress in the vicinity of the borehole at early time $t = 0.1$ s.
 40
 41
 42
 43
 44
 45
 46
 47
 48
 49
 50
 51
 52
 53
 54
 55
 56
 57
 58
 59
 60
 61
 62
 63
 64
 65

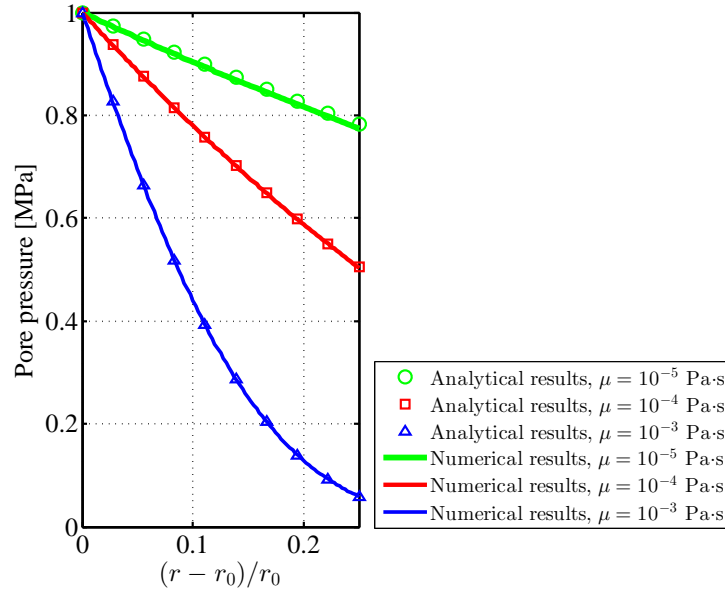


Figure 6: Poroelastic response of a borehole. The distribution of pore pressure caused by fluid pressurization is shown around the borehole for three different dynamic viscosities μ at early time $t = 0.1$ s. As seen, the results are in good accordance with the analytical in [55].

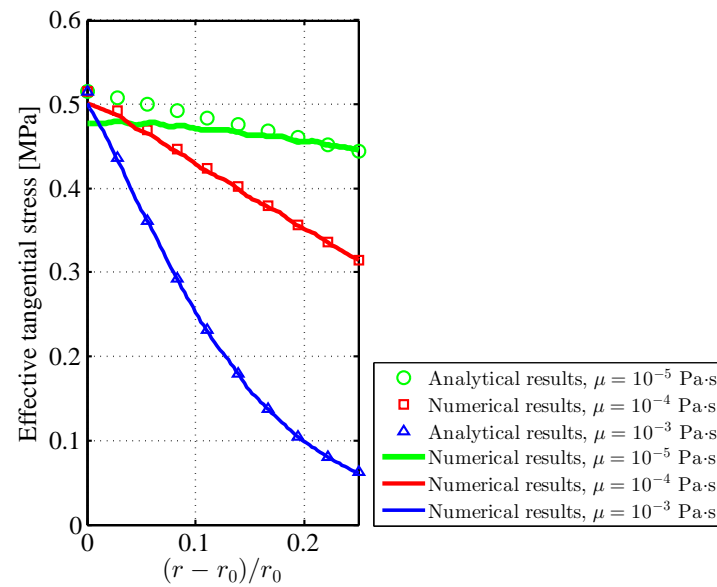


Figure 7: Poroelastic response of a borehole. The effective tangential stress is plotted near the borehole for three different dynamic viscosities μ at early time $t = 0.1$ s.

1
2
3
4
5
6
7
8
9 *4.3. Computation of the crack opening displacement*

10 We now focus on a classical problem first solved by Sneddon and Lowengrub
 11 [57] (see also [20]) that solves the opening displacement of a static line crack.

12 Consider a computational domain of $\Omega = 4 \text{ m} \times 4 \text{ m}$ with a preexisting line
 13 fracture of length $2a_0 = 0.4 \text{ m}$, i.e., $\mathcal{C} = [1.8, 2.2] \times \{0\}$. To minimize the effect
 14 of the boundary conditions on the results, the domain size is much larger than
 15 the crack length ($L \gg 2a_0$).

16 The mechanical properties of the material are the Young's modulus $E = 1000$
 17 MPa, the Poisson's ratio $\nu = 0$, and the fracture toughness $g_c = 1 \text{ MPa}\cdot\text{s}$.

18 We impose zero displacements on the external boundary of Ω . Also we set
 19 $d = 1$ on prescribed (initial) fracture and $d = 0$ on the external boundary of
 20 Ω . A monotonically increasing pressure is applied on the upper and lower faces
 21 of fracture with the magnitude $p = 1 \text{ MPa}$. Figure 8 depicts the geometry and
 22 boundary conditions.

23 Bourdin *et al.* [33] proposed a formula to compute the fracture aperture as:

$$w = \mathbf{u} \cdot \mathbf{n}_\Gamma \simeq \int_s \mathbf{u} \cdot \nabla d \, dx.$$

24 Then, the fracture volume is calculated by integrating the fracture aperture
 25 along the fracture's path:

$$V_f = \int_\Gamma w \, ds \simeq \int_\Omega \mathbf{u} \cdot \nabla d \, d\Omega.$$

26 Figure 9 shows the aperture profile for different h and ℓ . The dash line in
 27 black represents the Sneddon's analytical solution [57]. Also, the crack volume
 28 computed by Sneddon's analytical solution and our numerical tests are summa-
 29 rized in Table 3.

30 Table 3: Crack volumes for different ℓ for numerical tests and analytical solution ($h = 4\text{mm}$).

| ℓ (mm) | 1.4×10^2 | 1.2×10^2 | 1.0×10^2 |
|---|--------------------|--------------------|--------------------|
| Numerical fracture volume (mm ²) | 2.89×10^2 | 2.75×10^2 | 2.60×10^2 |
| Analytical fracture volume (mm ²) | 2.51×10^2 | | |

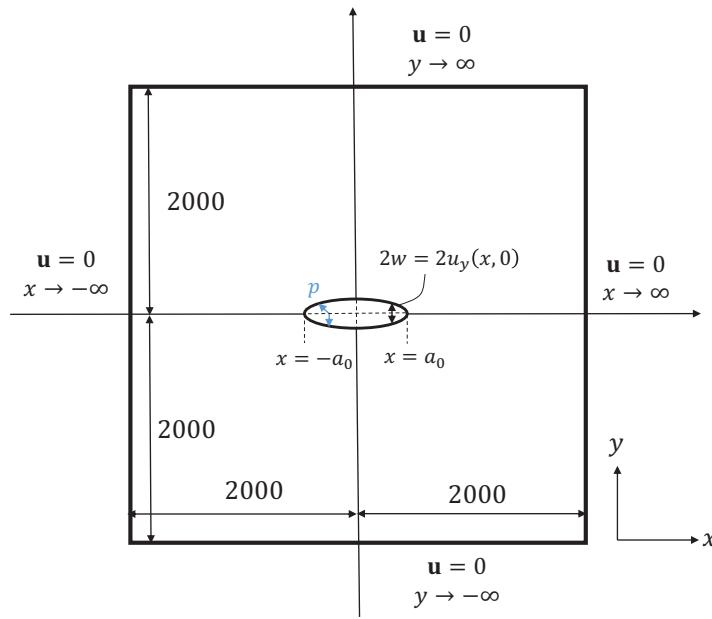


Figure 8: Computation of the crack opening displacement. Schematic view of the deformed line crack in a two dimensional domain.

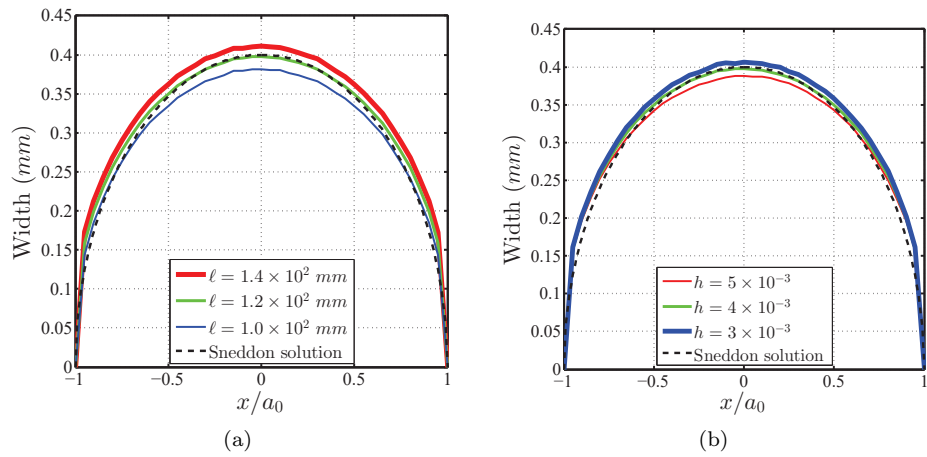
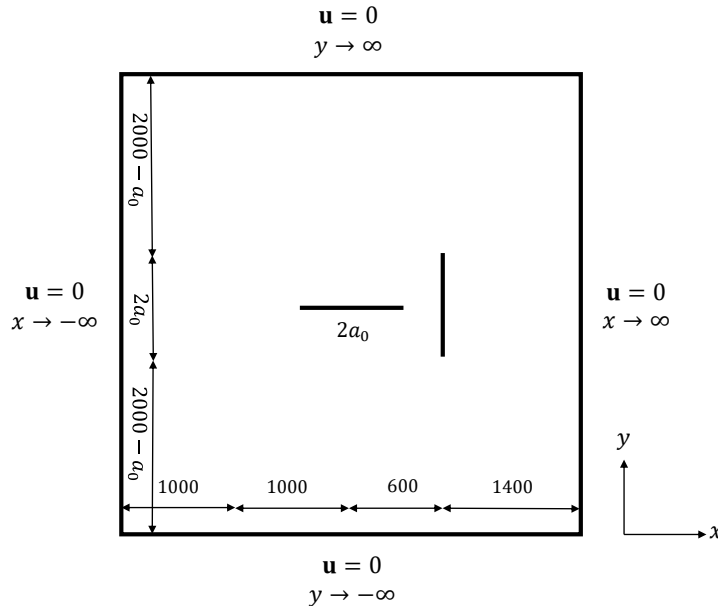


Figure 9: Computation of the crack opening displacement. We output the results for (9a) various ℓ with $h = 4 \text{ mm}$ and (9b) various h with $\ell = 1.2 \times 10^2 \text{ mm}$, and compare them with Sneddon's analytical solution [57].

1
2
3
4
5
6
7
8
9 4.4. Increasing pressure leading to joining fractures

10 This example motivated by Wheeler *et al.* [58] demonstrates one major capability
11 of the phase field approach that there is no need to track any complicated
12 fracture geometry for joining fractures.

13 Consider a computational domain of $\Omega = (0, 4.0) \times (0, 4.0)$ (unit: m by m)
14 containing two pre-existing line fractures with a length of $2a_0 = 0.4$ m, more
15 precisely, $\mathcal{C}_h = [1.8, 2.2] \times \{0\}$ and $\mathcal{C}_v = \{2.6\} \times [1.8, 2.2]$. To minimize the
16 effect of the boundary conditions on the results, the domain size is much bigger
17 than the fracture length ($L \gg 2a_0$). A discretization with 19,368 standard P_1
18 elements is applied such that an effective element size of $h \approx 20$ mm is obtained
19 in the critical zone. Also, let $\ell = 2h$. Figure 10 depicts the geometric setup.
20 A zero displacement is imposed on the boundary. Also, we set $d = 1$ for the
21 prescribed (initial) fractures, and $d = 0$ on the boundary. A monotonically
22 increasing pressure is applied on the upper and lower faces of the fracture with
23 the magnitude $p = m\bar{p}$ where $\bar{p} = 0.01$ MPa and $m = 1, 2, \dots, 115$.



47 Figure 10: Schematic of a square plate (unit: mm) with two pre-existing fractures. A monotonically
48 increasing pressure with constant increments $p = m\bar{p}$ is applied on the fracture
49 faces.

50 Following [58], we adopt the values of the material parameters given in Table
51 4.

52 Figure 11 shows the phase field evolution at different load steps: (11a) $m = 1$,
53 (11b) $m = 113$, (11c) $m = 114$, and (11d) $m = 115$. The results show that the
54 horizontal fracture starts to propagate at $m = 113$, and at $m = 114$ it intersects
55 the vertical fracture. Overall speaking the fracture paths agree with those in
56 [58]. Note the fracture propagation is unstable in this example.

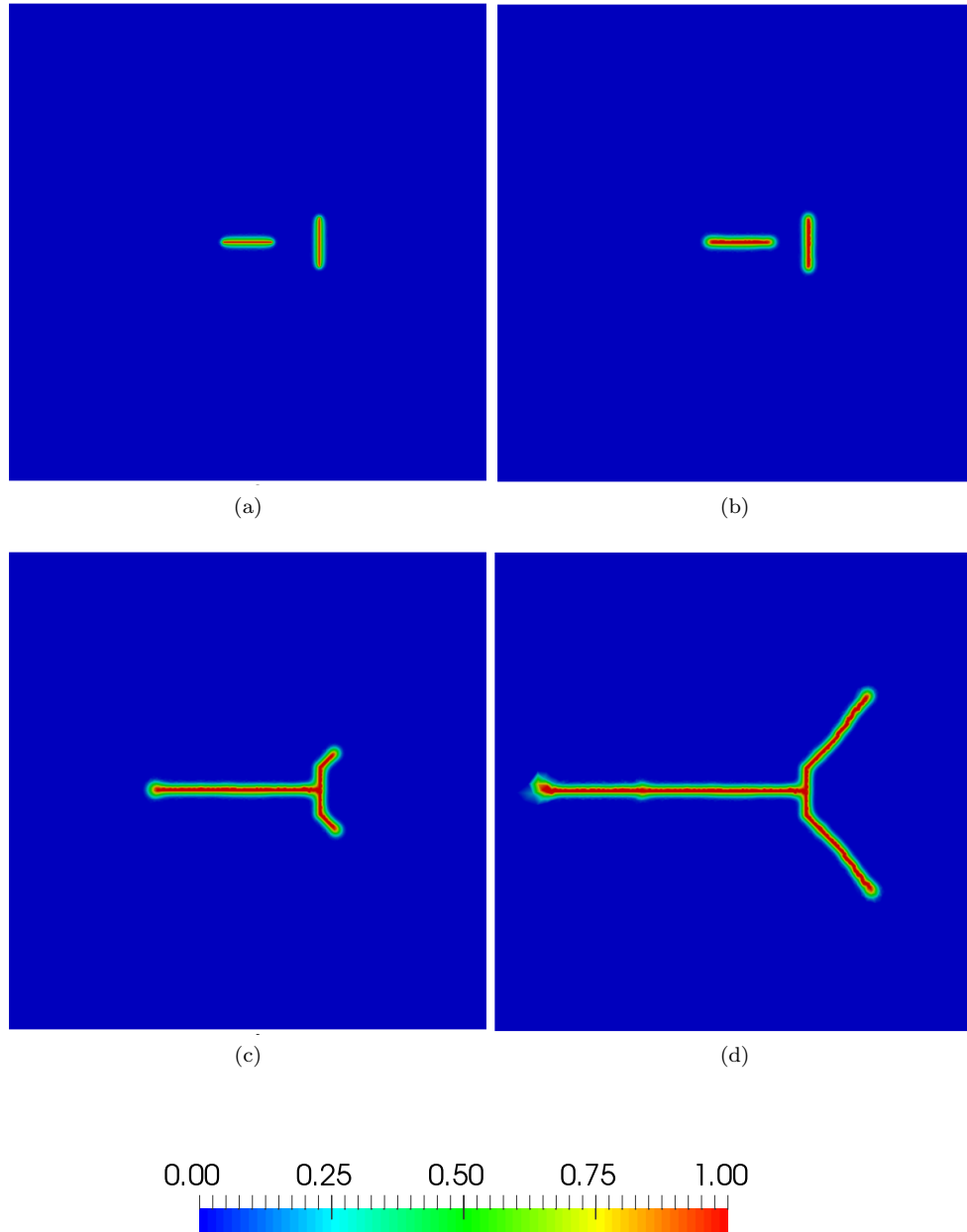


Figure 11: Increasing pressure leading to joining fractures ($p = m\bar{p}$). Phase field contours at different load steps (11a) $m = 1$, (11b) $m = 113$, (11c) $m = 114$, and (11d) $m = 115$. The results show that the horizontal fracture starts to propagate at $m = 113$, and at $m = 114$ it intersects the vertical fracture.

Table 4: Increasing pressure leading to joining fractures: Material parameters [58]

| Parameters | symbol | unit | value |
|------------------------------|--------|--------|-------|
| Young's modulus | E | MPa | 1.0 |
| Poisson's ratio | ν | — | 0.2 |
| Critical energy release rate | g_c | MPa·mm | 1.0 |

4.5. CO_2 -driven fracture

In this example, we investigate the fracture propagation in a square plate with a pressurized CO_2 flow, with [10, 11] as the benchmarks. The specimen has edge lengths of $L = 170$ mm. The geometric setup and boundary conditions are depicted in Figure 12. The sample is discretized into 4,832 three-noded triangular elements so that the mesh size $h \approx 5.68$ mm is obtained. Also, we set $\ell = 1.6$ mm. Table 5 shows the remaining parameters to be input.

$$\mathbf{u} = \mathbf{u}_D, p = p_D$$

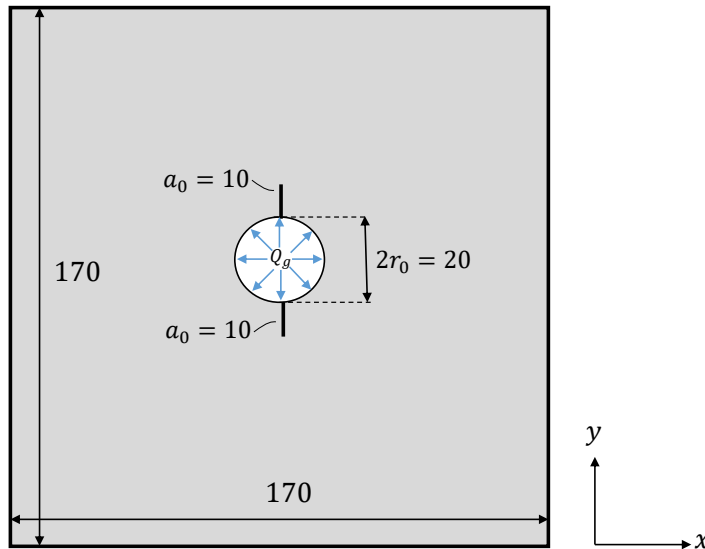


Figure 12: Schematic of a fractured square plate (unit: mm) with pressurized CO_2 flow.

As in Figure 12, there exist two preexisting fractures representing the perforations. We set $d = 1$ for both fractures and set the Dirichlet boundary condition $d = 0$ on the external boundary. The fluid is continuously injected into the central borehole with diameter $2r_0 = 20$ mm, until after the fractures propagate. Note that in this problem, the isothermal condition is adopted so that CO_2 is in the supercritical phase ($T = 45^\circ C$).

For the sake of simplicity, the *in situ* stress $\sigma_1 = \sigma_3 = 1$ MPa is imposed on the boundary by means of its “equivalent” prescribed displacement. More precisely, the displacement of the same specimen with no fracture under the

same *in situ* stress is first computed, then used as the Dirichlet boundary condition for the problem at hand. On the external boundary, we set $p = p_D$ where $p_D = 0$. Moreover, $\Gamma_P = \Gamma_D$ in this example.

Table 5: Default parameter values for the example. These values are taken from [11] except g_c , which is from (6).

| Parameters | symbol | unit | value |
|--------------------------------------|------------|-----------------|------------------------|
| Young's modulus | E | MPa | 6×10^3 |
| Poisson's ratio | ν | — | 0.34 |
| Critical energy release rate | g_c | MPa·mm | 0.306 |
| Biot coefficient | α | — | 0.85 |
| Porosity | ϕ | — | 0.01 |
| Initial permeability | k_0 | mm ² | 1×10^{-12} |
| Dynamic viscosity of CO ₂ | μ | MPa·s | 4.04×10^{-11} |
| Initial pressure | p_0 | MPa | 0.1 |
| Rock's tensile strength | σ_T | MPa | 11 |

Figure 13 shows the evolution of phase field diagram (left) and pressure profile (right) at different time steps. As seen, the fractures propagate along a straight line, and the pressure profile is accordingly distributed with the highest gradient around the borehole.

Next, we aim to calculate the breakdown pressure p_b , the pressure value when the fractures start to propagate. Figure 14 illustrates the pressure evolution at the top of the borehole and the fracture length function. To estimate the breakdown pressure, first we output the fracture length with regard to (2). Then, we obtain the time when the slope suddenly changes in the fracture length function (\mathcal{C}_ℓ), which is the time corresponding to the breakdown pressure (here $t \approx 0.72t_f$). Hence the breakdown pressure reads $p_b = 10.9$ MPa. This value for p_b is in agreement with H-F and H-W analytical solutions. Also, our results agree with experiments results of Ishida *et al.* [9] within 30%, see Table 6 and the next paragraph for more elaborations.

Table 6: Breakdown pressure of numerical test and analytical solutions for $\sigma_1 = \sigma_3 = 1$ MPa.

| | Numerical | H-F solution | H-W solution | Experimental [9] |
|-------------|-----------|--------------|--------------|------------------|
| p_b (MPa) | 10.9 | 11 | 9.1 | 8.44 |

Classical solutions of breakdown pressure. There exist two classical expressions to calculate the breakdown pressure. In the case without poroelastic effect the rock deformation does not penetrate into the pressurized fracture, the Hubbert-Willis (H-W) solution applies [59]:

$$p_b = 3\sigma_3 - \sigma_1 + \sigma_T,$$

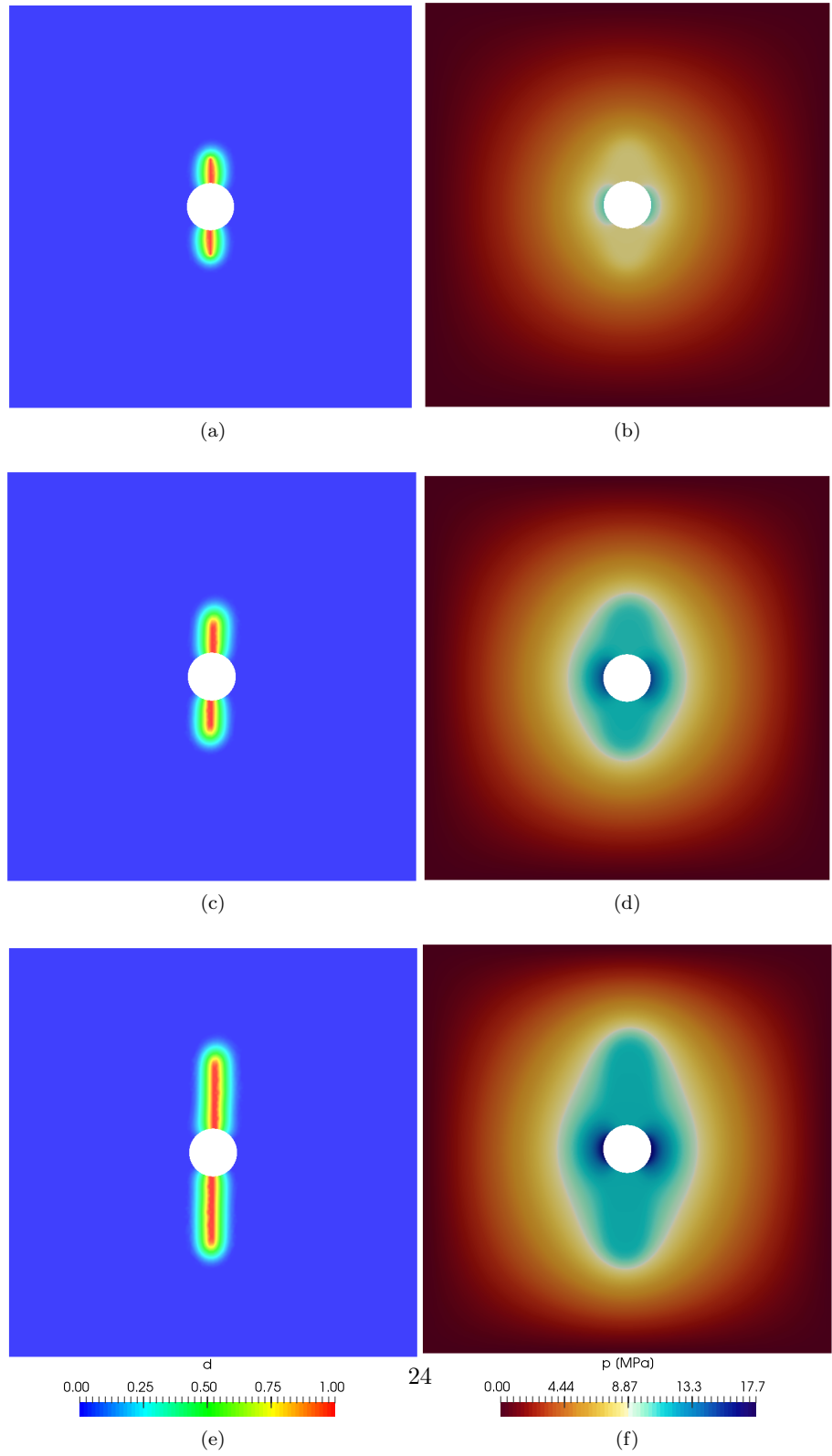


Figure 13: Left: Phase field diagram at different stages (13a) $t = 0.5t_f$, (13c) $t = 0.74t_f$, and (13e) $t = t_f$. Right: Pressure profile at (13b) $t = 0.5t_f$, (13d) $t = 0.74t_f$, and (13f) $t = t_f$.

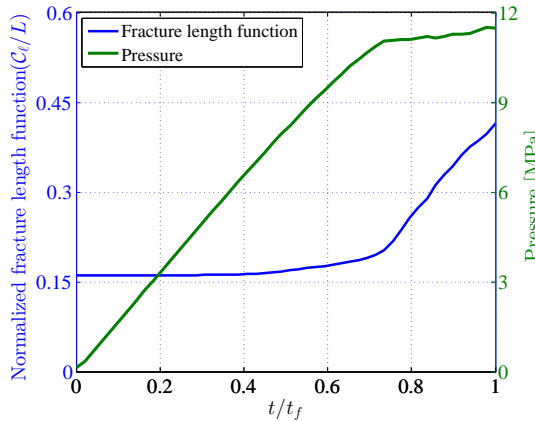


Figure 14: The pressure at the top of the borehole (green line), and the fracture length function (blue line) as functions of time. The time when there is a sudden change of slope in C_ℓ assumes the time corresponding to the breakdown pressure ($t = 0.72t_f$) and the corresponding breakdown pressure is $p_b = 10.9$ MPa. This is in agreement with H-F and H-W analytical solutions.

in which the rock is assumed to be an elastic medium. When the porous medium is set, the Haimson-Fairhurst (H-F) solution is preferred [60]:

$$p_b = \frac{3\sigma_3 - \sigma_1 + \sigma_T + p_0}{1 + \frac{\nu}{1-\nu}\alpha},$$

where we denote by p_b the breakdown fluid pressure, σ_3 , and σ_1 are the minimum and maximum principal stresses, respectively, and σ_T is the rock's tensile strength.

Effect of N , h , and ℓ on the breakdown pressure. Here we aim to study how the number of time steps N , the mesh size h , and the regularization length scale ℓ affect the value of breakdown pressure. As seen in Figure 15, the plots show similar numerical results for the pressure evolution.

Breakdown pressure result of an anisotropic in situ stress. In this example we set the maximum ($\sigma_1 = 3$ MPa) and minimum ($\sigma_3 = 2$ MPa) *in situ* stress. The other input data and boundary conditions are the same as aforementioned.

The pressure at the top of the borehole and the fracture length function, (2), at different stages are illustrated in Figure 16. The breakdown time ($t \approx 0.77t_f$) and the corresponding breakdown pressure is $p_b = 11.9$ MPa, see Table 7.

Table 7: Breakdown pressure of numerical test and analytical solutions for $\sigma_1 = 3$ MPa and $\sigma_3 = 2$ MPa.

| | Numerical | H-F solution | H-W solution |
|-------------|-----------|--------------|--------------|
| p_b (MPa) | 11.9 | 14 | 9.8 |

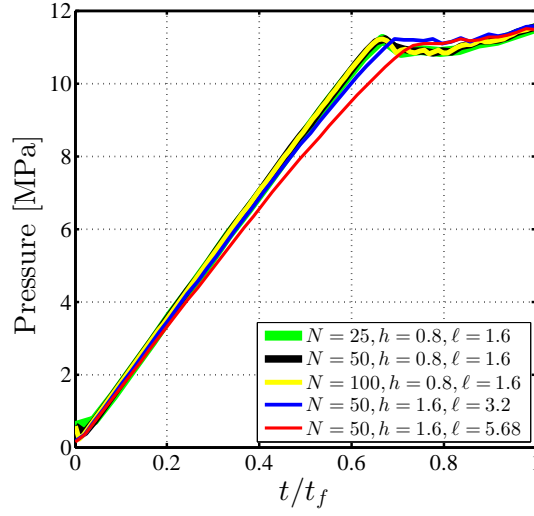


Figure 15: Evolution of the pressure at the top of the borehole for different numbers of time steps N , mesh size h , and ℓ .

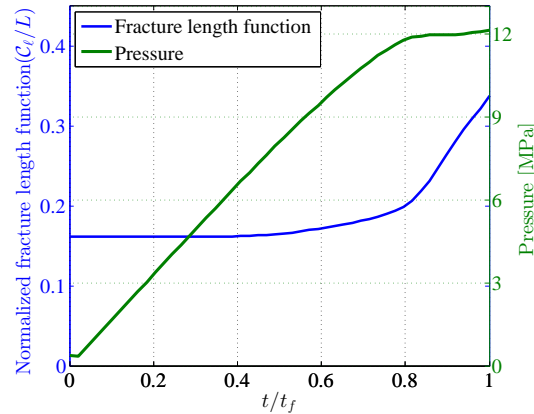


Figure 16: The pressure at the top of the borehole (green line) and the fracture length function (blue line) versus time for deviatoric *in situ* stress are shown. The time ($t \approx 0.8t_f$) when there is a change of slope in the fracture length function (C_ℓ) should correspond to the breakdown pressure ($p_b = 11.9$ MPa).

1
 2
 3
 4
 5
 6
 7
 8
 9
 10
 11
 12
 13
 14
 15
 16
 17
 18
 19
 20
 21
 22
 23
 24
 25
 26
 27
 28
 29
 30
 31
 32
 33
 34
 35
 36
 37
 38
 39
 40
 41
 42
 43
 44
 45
 46
 47
 48
 49
 50
 51
 52
 53
 54
 55
 56
 57
 58
 59
 60
 61
 62
 63
 64
 65

Effect of dynamic viscosity on breakdown pressure. We conduct several numerical examples to investigate the effect of dynamic viscosity μ on the breakdown pressure p_b . In this set of examples an effective mesh size, the mesh size near the borehole or the fractures, $h \approx 1.6$ mm is adopted. Also, we set $\ell = 2h$. In Figure 17 we plot the pressure evolution up to the time when $C_\ell(t)$ changes slope, so that the end points correspond to the breakdown pressures. The results indicate that p_b is approximately the same for different fluid viscosities, but the time when breakdown pressure reaches is different. Figure 17 demonstrates that the rock will break earlier for the fluid with bigger dynamic viscosity. Also it shows that regardless of the fracturing fluid, the breakdown pressure is slightly the same for all cases. This is in accordance with the physics that the breakdown pressure normally reflects the strength of the solid. However, Wang *et al.* [11] reported different breakdown pressures for different fluids which also agrees with some experiments [9, 10]. We believe this discrepancy demands further research.

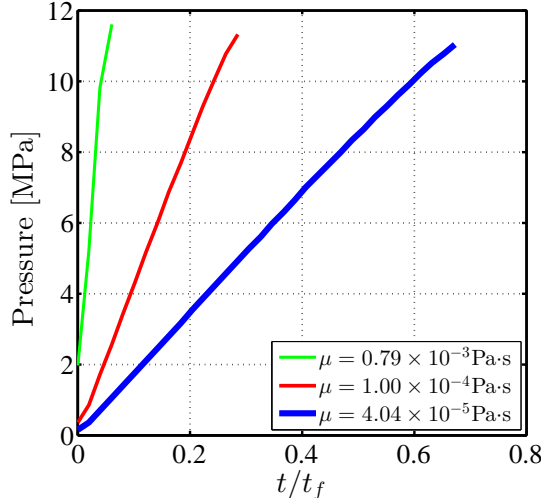


Figure 17: Evolution of the pressure at the top of the borehole for different μ 's. As seen, even though p_b is the same for different fracturing fluids, by increasing μ , the breakdown pressure is reached earlier.

4.6. Interaction between CO₂-driven fractures and natural fractures

In this example, we investigate the interaction between two CO₂-driven fractures and two inclined natural fractures. The specimen has edge lengths of $L = 170$ mm. The geometric setup and boundary conditions are depicted in Figure 18. The sample is discretized into 32,736 three-noded triangular elements so that the mesh size $h \approx 6.25 \times 10^{-1}$ mm is obtained. Also, we set $\ell = 4h$. The remaining input data can be found in Table 5.

As in Figure 18, there exist two pre-existing vertical fractures representing the perforations and two inclined natural fractures. We set $d = 1$ for both initial and inclined natural fractures, and the Dirichlet boundary condition $d = 0$ is

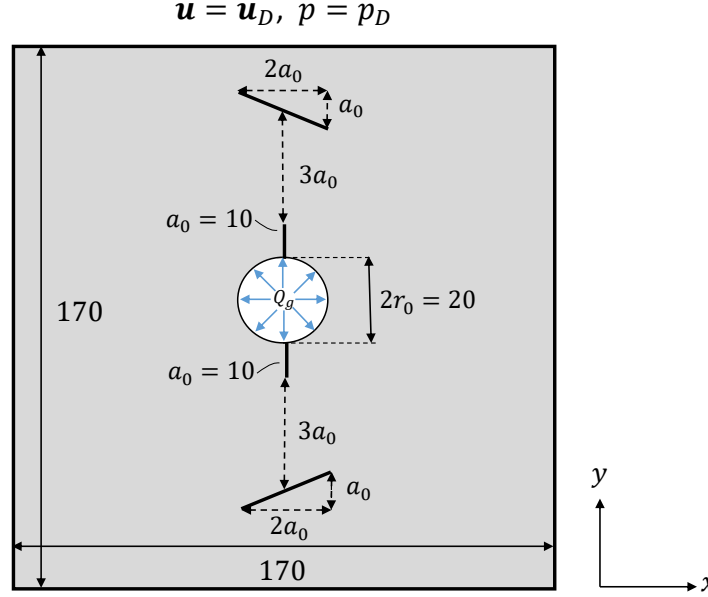


Figure 18: Interaction between CO₂-driven fracture and inclined natural fractures. The geometric setup and boundary conditions are shown (unit: mm). There exist two CO₂-driven fractures and two inclined natural ones.

imposed on the external boundaries. The fluid is continuously injected into the central borehole with diameter $2r_0 = 20$ mm. The *in situ* stress with the value of $\sigma_1 = \sigma_3 = 1$ MPa is also imposed on the boundary by means of its ‘equivalent’ prescribed displacement. See Section 4.5 for more descriptions.

Figure 19 shows the evolution of the phase field profile (left) and the pressure profile (right) at different time steps. As seen, the vertical fractures propagate along a straight line until $t = 0.4t_f$. Then, near the inclined natural fractures, the CO₂-driven fractures turns to join them with an angle of approximately 90° at $t = 0.8t_f$. In the last frame 19g, the vertical fractures deviate into the inclined natural fractures and propagate from left tips. This fracture evolving pattern is called ‘crossing with an offset’ which is one possible interaction process of hydraulic fracture and natural fracture [61].

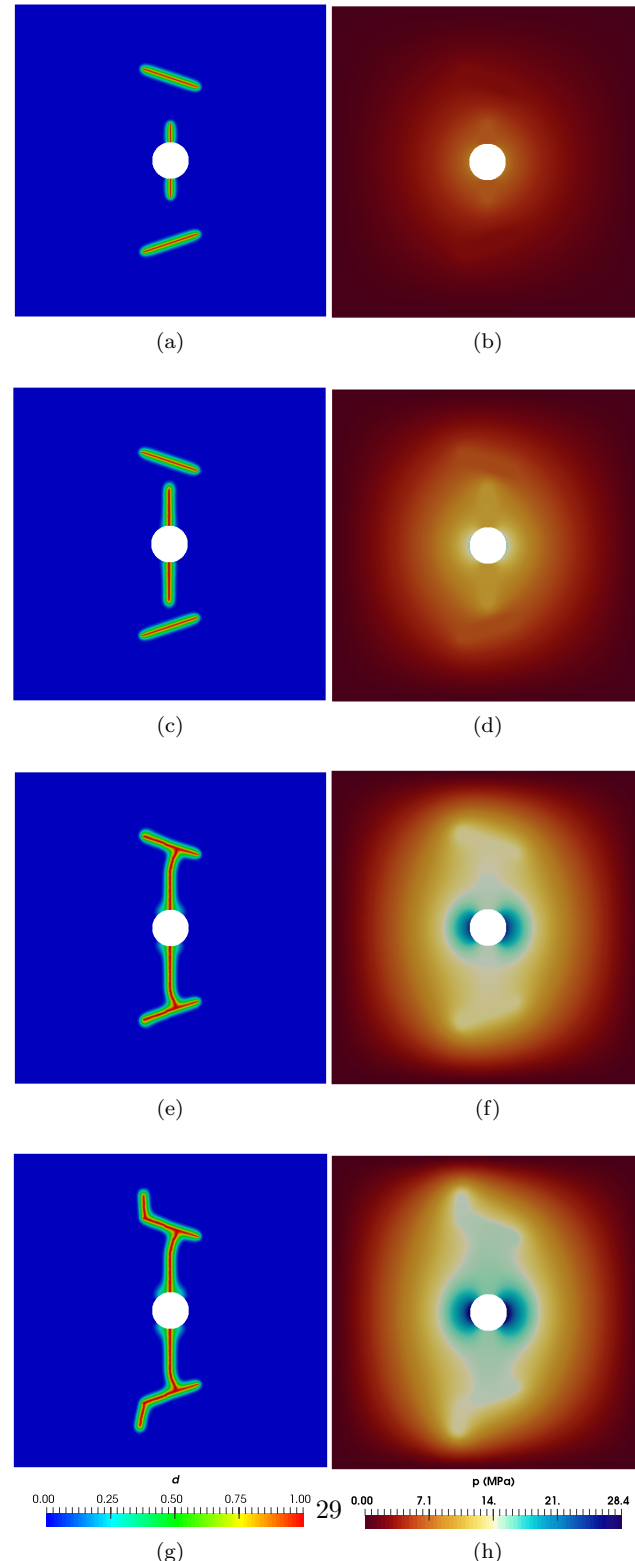


Figure 19: Left: Phase field diagram at different stages (19a) $t = 0.$, (19c) $t = 0.4t_f$, (19e) $t = 0.8t_f$, and (19g) $t = t_f$. Right: Pressure profile at (19b) $t = 0.$, (19d) $t = 0.4t_f$, (19f) $t = 0.8t_f$, and (19h) $t = t_f$. As seen, the vertical fractures propagate along a straight line until they reached the natural fractures. Then, they deviate into the inclined natural fractures, and continue evolving from left tips. ‘Crossing with an offset’ is one possible interaction process of hydraulic fracture and natural fracture [61].

1
2
3
4
5
6
7
8
9
10 **410 5. Conclusions**

11 We have proposed **and verified** a phase field approach to simulate CO₂ frac-
12 turing, with CO₂ treated as a compressible fluid. **In one of the numerical ex-**
13 **amples, the**~~The~~ breakdown pressure agrees well with widely used analytical
14 solutions. Also, the results agree with experimental results within 30%. While
15 this work represents the first of its kind, potentially the phase field approach
16 allows complicated modeling of fracture initiation and branching.
17
18
19
20
21
22
23
24
25
26
27
28
29
30
31
32
33
34
35
36
37
38
39
40
41
42
43
44
45
46
47
48
49
50
51
52
53
54
55
56
57
58
59
60
61
62
63
64
65

AppendixA. Weak forms and discretized formulations

Here we provide weak forms useful for FEniCS implementation.

AppendixA.1. Porous medium

To proceed, let the test function spaces be

$$\begin{aligned}\mathcal{V}_u &:= \{\bar{\mathbf{u}} \in H^1(\Omega; \mathbb{R}^2) \mid \bar{\mathbf{u}} = \mathbf{0} \text{ on } \Gamma_D\}, \\ \mathcal{V}_d &:= H^1(\Omega).\end{aligned}$$

Then we derive the first variations of the energy functional (3), which will be needed for stating the weak form:

$$\begin{aligned}\delta\Pi_\ell [(\mathbf{u}, d); \bar{\mathbf{u}}] &:= \int_{\Omega} \boldsymbol{\sigma}[\boldsymbol{\varepsilon}(\mathbf{u}), d] : \boldsymbol{\varepsilon}(\bar{\mathbf{u}}) \, d\Omega - \int_{\Gamma_N} \mathbf{t}_N \cdot \bar{\mathbf{u}} \, d\Gamma - \int_{\Omega} \mathbf{b} \cdot \bar{\mathbf{u}} \, d\Omega \\ &\quad + \int_{\Omega} (\alpha - 1) \nabla ((1 - d)^2 p) \cdot \bar{\mathbf{u}} \, d\Omega + \int_{\Omega} (1 - d)^2 \nabla p \cdot \bar{\mathbf{u}} \, d\Omega\end{aligned}\tag{A.1a}$$

$$\begin{aligned}\delta\Pi_\ell [(\mathbf{u}, d); \bar{d}] &:= \int_{\Omega} (\alpha - 1) g'(d) \bar{d} p \operatorname{div} \mathbf{u} \, d\Omega + \int_{\Omega} g'(d) \bar{d} \nabla p \cdot \mathbf{u} \, d\Omega \\ &\quad + \int_{\Omega} g'(d) \psi_+(\boldsymbol{\varepsilon}) \bar{d} \, d\Omega + \frac{g_c}{4c_w} \int_{\Omega} \left(\frac{\omega'(d) \bar{d}}{\ell} + 2\ell \nabla d \cdot \nabla \bar{d} \right) \, d\Omega.\end{aligned}\tag{A.1b}$$

The weak form can thus be stated as: Find $(\mathbf{u} \times d) \in \mathcal{S}_{\mathbf{u}} \times \mathcal{S}_d$, such that for all admissible functions $(\bar{\mathbf{u}} \times \bar{d}) \in \mathcal{V}_{\mathbf{u}} \times \mathcal{V}_d$, $\delta\Pi_\ell [(\mathbf{u}, d); \bar{\mathbf{u}}] = 0$ and $\delta\Pi_\ell [(\mathbf{u}, d); \bar{d}] = 0$.

Also we take another variation from (3) which will be needed for the discretized formulation:

$$\delta^2\Pi_\ell [(\mathbf{u}, d); \bar{\mathbf{u}}, \delta\mathbf{u}] = \int_{\Omega} \boldsymbol{\varepsilon}(\delta\mathbf{u}) : \mathbb{C}[\boldsymbol{\varepsilon}(\mathbf{u}), d] : \boldsymbol{\varepsilon}(\bar{\mathbf{u}}) \, d\Omega,\tag{A.2a}$$

$$\begin{aligned}\delta^2\Pi_\ell [(\mathbf{u}, d); \bar{d}, \delta d] &= \int_{\Omega} \delta d \, g''(d) \psi_+(\boldsymbol{\varepsilon}) \bar{d} \, d\Omega \\ &\quad + \int_{\Omega} (\alpha - 1) g''(d) \bar{d} \, \delta d \, p \operatorname{div} \mathbf{u} \, d\Omega + \int_{\Omega} g''(d) \bar{d} \, \delta d \, \nabla p \cdot \mathbf{u} \, d\Omega \\ &\quad + \frac{g_c}{4c_w} \int_{\Omega} \left[\frac{\delta d \, w''(d) \bar{d}}{\ell} + 2\ell \nabla(\delta d) \cdot \nabla \bar{d} \right] \, d\Omega,\end{aligned}\tag{A.2b}$$

where the fourth-order tensor $\mathbb{C}[\boldsymbol{\varepsilon}(\mathbf{u}), d] = \frac{\partial \boldsymbol{\sigma}(\boldsymbol{\varepsilon}, d)}{\partial \boldsymbol{\varepsilon}} \Big|_{\boldsymbol{\varepsilon}=\boldsymbol{\varepsilon}(\mathbf{u})}$ is the tangent elasticity tensor.

To discretize the problem, we divide Ω with a conforming mesh \mathcal{T}_h of triangular elements. Let η be the set of nodes of \mathcal{T}_h . We approximate (\mathbf{u}, d) with the standard P_1 finite element basis functions associated with all nodes $i \in \eta$:

$$\mathbf{u}(\mathbf{x}) = \sum_{i \in \eta} \mathbf{N}_i^{\mathbf{u}}(\mathbf{x}) \mathbf{u}_i, \quad d(\mathbf{x}) = \sum_{i \in \eta} N_i(\mathbf{x}) d_i,\tag{A.3}$$

where \mathbf{u}_i , and d_i are the displacement and phase field values at node i , respectively; and $\mathbf{N}_i^{\mathbf{u}}$ is given by:

$$\mathbf{N}_i^{\mathbf{u}} = \begin{bmatrix} N_i & 0 \\ 0 & N_i \end{bmatrix},$$

where N_i is the standard finite element shape function associated with $i \in \eta$, satisfying $N_j(\mathbf{x}_i) = \delta_{ji}$, for all $i, j \in \eta$, and $\mathbf{x}_i, \mathbf{u}_i \in \mathbb{R}^2$ are the position vector and nodal displacement vector of node i , respectively. Note that we also apply the same discretization to the test functions.

Discretized weak form. Let n_{nodes} denote the number of nodes in η . Let $\mathbf{u} \in \mathbb{R}^{2n_{\text{nodes}}}$, $\mathbf{d} \in \mathbb{R}^{n_{\text{nodes}}}$ contain all entries of \mathbf{u}_i , d_i , respectively, for all $i \in \eta$. The discretized residuals can be written as $\mathbb{U}_i(\mathbf{u}) := \delta\Pi(\mathbf{u}; \mathbf{N}_i^{\mathbf{u}}) \in \mathbb{R}^2$ and $\mathbb{D}_i(d) := \delta\Pi(d; N_i) \in \mathbb{R}$ for all $i \in \eta$. With (A.1), these residual vectors are expressed as follows:

$$\begin{aligned} \mathbb{U}_i &= \int_{\Omega} (\mathbf{B}_i)^T \boldsymbol{\sigma}[\boldsymbol{\varepsilon}(\mathbf{u}), d] d\Omega - \int_{\Gamma_N} (\mathbf{N}_i^{\mathbf{u}})^T \mathbf{t}_N d\Gamma - \int_{\Omega} (\mathbf{N}_i^{\mathbf{u}})^T \mathbf{b} d\Omega \\ &\quad + \int_{\Omega} (\alpha - 1)(\mathbf{N}_i^{\mathbf{u}})^T \nabla ((1 - d)^2 p) d\Omega + \int_{\Omega} (\mathbf{N}_i^{\mathbf{u}})^T (1 - d)^2 \nabla p d\Omega \\ \mathbb{D}_i &= \int_{\Omega} (\alpha - 1) g'(d) N_i p \operatorname{div} \mathbf{u} d\Omega + \int_{\Omega} g'(d) N_i (\nabla p)^T \mathbf{u} d\Omega \\ &\quad + \int_{\Omega} g'(d) \psi_+(\boldsymbol{\varepsilon}) N_i d\Omega + \frac{g_c}{4c_w} \int_{\Omega} \left(\frac{w'(d) N_i}{\ell} + 2\ell \nabla d \cdot \nabla N_i \right) d\Omega, \end{aligned} \quad (\text{A.4})$$

where \mathbb{U}_i is also called the nodal force at i . Also note that in (A.4), $\boldsymbol{\sigma}$ is understood as a 3-vector, and the strain-displacement matrix for node i are given by:

$$\mathbf{B}_i = \begin{bmatrix} N_{i,x} & 0 \\ 0 & N_{i,y} \\ N_{i,y} & N_{i,x} \end{bmatrix}.$$

The discretized weak form is $\mathbb{U}_i = \mathbf{0}$ for all nodes i at which \mathbf{u} is not prescribed, and $\mathbb{D}_i = 0$ for all nodes i at which d is not prescribed.

Tangent stiffness matrices. The tangent stiffness matrices are needed for Newton-Raphson algorithms. The tangent stiffness matrix components of (A.2) are $\mathbf{K}_{ij}^u := \partial \mathbb{U}_i / \partial \mathbf{u}_j = \delta^2 \Pi[\mathbf{u}; \mathbf{N}_i^{\mathbf{u}}, \mathbf{N}_j^{\mathbf{u}}] \in \mathbb{R}^{2 \times 2}$ for all $i, j \in \eta$ and $K_{ij}^d := \partial \mathbb{D}_i / \partial d_j = \delta^2 \Pi[d; N_i, N_j] \in \mathbb{R}$ for all $i, j \in \eta$, which can be expressed as follows:

$$\mathbf{K}_{ij}^u = \int_{\Omega} (\mathbf{B}_i)^T \mathbf{D} \mathbf{B}_j d\Omega, \quad (\text{A.5a})$$

$$\begin{aligned} K_{ij}^d &= \int_{\Omega} (\alpha - 1) g''(d) N_i N_j p \operatorname{div} \mathbf{u} d\Omega + \int_{\Omega} g''(d) N_i N_j (\nabla p)^T \mathbf{u} d\Omega \\ &\quad + \int_{\Omega} g''(d) \psi_+(\boldsymbol{\varepsilon}) N_i N_j d\Omega + \frac{g_c}{4c_w} \int_{\Omega} \left[\frac{w''(d) N_i N_j}{\ell} + 2\ell (\nabla N_i)^T \nabla N_j \right] d\Omega, \end{aligned} \quad (\text{A.5b})$$

where we denote by \mathbf{D} the matrix form of the tangent elastic modulus tensor \mathbb{C} . Below we give its expression $\mathbf{D} = g(d)\mathbf{D}_+ + \mathbf{D}_-$ for our adopted tension-compression decomposition [34]:

$$\mathbf{D}_+ = BH(\text{tr } \boldsymbol{\varepsilon}) \begin{bmatrix} 1 & 1 & 0 \\ 1 & 1 & 0 \\ 0 & 0 & 0 \end{bmatrix} + \frac{G}{3} \begin{bmatrix} 4 & -2 & 0 \\ -2 & 4 & 0 \\ 0 & 0 & 3 \end{bmatrix},$$

$$\mathbf{D}_- = BH(-\text{tr } \boldsymbol{\varepsilon}) \begin{bmatrix} 1 & 1 & 0 \\ 1 & 1 & 0 \\ 0 & 0 & 0 \end{bmatrix},$$

where $B = E/[3(1-2\nu)]$ is the bulk modulus. Here, H is the Heaviside function such that $H(a) = 1$ if $a > 0$, $H(a) = 0$ if $a < 0$, and $H(a) = \frac{1}{2}$ if $a = 0$.

Appendix A.2. Compressible (CO_2) fluid flow discretization

The compressible fluid flow discretization is also done via the finite element method. We first discretize in time and then in space. We will adopt the backward Euler method for time discretization.

To proceed, let the admissible set of pressure be:

$$\mathcal{S}_p := \{p \in H^1(\Omega) \mid p = p_D \text{ on } \Gamma_P\}.$$

The test function space can be defined as:

$$\mathcal{V}_p := \{\bar{p} \in H^1(\Omega) \mid \bar{p} = 0 \text{ on } \Gamma_P\}.$$

The weak form can be stated as: find $p \in \mathcal{S}_p$ such that for all admissible functions $\bar{p} \in \mathcal{V}_p$,

$$\begin{aligned} & \frac{1}{\Delta t} \int_{\Omega} \phi(\rho - \rho^{n-1}) \bar{p} \, d\Omega + \frac{1}{\Delta t} \int_{\Omega} \rho(\varepsilon_v - \varepsilon_v^{n-1}) \bar{p} \, d\Omega \\ & + \int_{\Omega} \rho \frac{k(d)}{\mu} \nabla p \cdot \nabla \bar{p} \, d\Omega - \int_{\Gamma_B} Q_g \bar{p} \, d\Gamma = 0, \end{aligned} \quad (\text{A.6})$$

where ρ^{n-1} and ε_v^{n-1} denote solutions at the previous time step.

Also, we use the conventional finite element shape functions $\{N_i\}$ for p :

$$p(\mathbf{x}) = \sum_{i \in \eta} p_i N_i(\mathbf{x}). \quad (\text{A.7})$$

Thus, the residual vector form of A.6 is expressed as follows:

$$\begin{aligned} \mathbb{P}_i := & \frac{1}{\Delta t} \int_{\Omega} \phi(\rho - \rho^{n-1}) N_i \, d\Omega + \frac{1}{\Delta t} \int_{\Omega} \rho(\varepsilon_v - \varepsilon_v^{n-1}) N_i \, d\Omega \\ & + \int_{\Omega} \rho \frac{k(d)}{\mu} (\nabla p)^T \nabla N_i \, d\Omega - \int_{\Gamma_B} Q_g N_i \, d\Gamma. \end{aligned} \quad (\text{A.8})$$

The discretized weak form is $\mathbb{P}_i = 0$ for all nodes i at which p is not prescribed.

The tangent stiffness matrix form of the fluid flow $K_{ij}^p := \partial \mathbb{P}_i / \partial p_j$ for all $i, j \in \eta$, which can be expressed as follows:

$$K_{ij}^p := \int_{\Omega} \rho \frac{k(d)}{\mu} (\nabla N_i)^T \nabla N_j \, d\Omega. \quad (\text{A.9})$$

1
2
3
4
5
6
7
8
9
10
11
12
13
14
15
16
17
18
19
20
21
22
23
24
25
26
27
28
29
30
31
32
33
34
35
36
37
38
39
40
41
42
43
44
45
46
47
48
49
50
51
52
53
54
55
56
57
58
59
60
61
62
63
64
65

Acknowledgments

140 This work is supported by the National Natural Science Foundation of China
with grant #11402146. YS also acknowledges the financial support by the Young
1000 Talent Program of China.

- 145 [1] G. Hattori, J. Trevelyan, C. E. Augarde, W. M. Coombs, A. C. Aplin, Numerical simulation of fracking in shale rocks: Current state and future approaches, *Archives of Computational Methods in Engineering* 24 (2) (2017) 281–317.
- 190 [2] R. Middleton, H. Viswanathan, R. Currier, R. Gupta, CO₂ as a fracturing fluid: Potential for commercial-scale shale gas production and CO₂ sequestration, *Energy Procedia* 63 (2014) 7780–7784.
- 235 [3] L. Wang, B. Yao, M. Cha, N. B. Alqahtani, T. W. Patterson, T. J. Kneafsey, J. L. Miskimins, X. Yin, Y.-S. Wu, Waterless fracturing technologies for unconventional reservoirs—opportunities for liquid nitrogen, *Journal of Natural Gas Science and Engineering* 35 (2016) 160–174.
- 280 [4] J. Miller, R. T. Johansen, Fracturing oil shale with explosives for in situ recovery, *Shale Oil, Tar Sands, and Related Fuel Sources* (1976) 98–111.
- 325 [5] A. T. Lillies, S. R. King, Sand fracturing with liquid carbon dioxide, in: SPE Production Technology Symposium, Society of Petroleum Engineers, 1982, pp. SPE-11341-MS.
- 370 [6] Y. Suehiro, M. Nakajima, K. Yamada, M. Uematsu, Critical parameters of { $x\text{CO}_2 + (1 - x)\text{CHF}_3$ } for $x = (1.0000, 0.7496, 0.5013, \text{ and } 0.2522)$, *The Journal of Chemical Thermodynamics* 28 (10) (1996) 1153–1164.
- 415 [7] D. W. Brown, A hot dry rock geothermal energy concept utilizing supercritical CO₂ instead of water, in: Proceedings of the twenty-fifth workshop on geothermal reservoir engineering, Stanford University, 2000, pp. 233–238.
- 460 [8] R. S. Middleton, J. W. Carey, R. P. Currier, J. D. Hyman, Q. Kang, S. Karra, J. Jiménez-Martínez, M. L. Porter, H. S. Viswanathan, Shale gas and non-aqueous fracturing fluids: Opportunities and challenges for supercritical CO₂, *Applied Energy* 147 (2015) 500–509.
- 505 [9] T. Ishida, K. Aoyagi, T. Niwa, Y. Chen, S. Murata, Q. Chen, Y. Nakayama, Acoustic emission monitoring of hydraulic fracturing laboratory experiment with supercritical and liquid CO₂, *Geophysical Research Letters* 39 (16) (2012) L16309.
- 550 [10] T. Ishida, Y. Chen, Z. Bennour, H. Yamashita, S. Inui, Y. Nagaya, M. Naoi, Q. Chen, Y. Nakayama, Y. Nagano, Features of CO₂ fracturing deduced from acoustic emission and microscopy in laboratory experiments, *Journal of Geophysical Research: Solid Earth* 121 (11) (2016) 8080–8098.

- [11] J. Wang, D. Elsworth, Y. Wu, J. Liu, W. Zhu, Y. Liu, The influence of fracturing fluids on fracturing processes: A comparison between water, oil and SC-CO₂, *Rock Mechanics and Rock Engineering* 51 (1) (2018) 299–313.
- [12] X. Zhou, T. J. Burbey, Fluid effect on hydraulic fracture propagation behavior: A comparison between water and supercritical CO₂-like fluid, *Geofluids* 14 (2) (2014) 174–188.
- [13] D. Ngo, A. C. Scordelis, Finite element analysis of reinforced concrete beams, *International Concrete Abstracts Portal* 64 (3) (1967) 152–163.
- [14] N. Moës, J. Dolbow, T. Belytschko, A finite element method for crack growth without remeshing, *International Journal for Numerical Methods in Engineering* 46 (1) (1999) 131–150.
- [15] R. Rangarajan, M. M. Chiaramonte, M. J. Hunsweck, Y. Shen, A. J. Lew, Simulating curvilinear crack propagation in two dimensions with universal meshes, *International Journal for Numerical Methods in Engineering* 102 (3-4) (2015) 632–670.
- [16] C. V. Verhoosel, M. A. Scott, T. J. Hughes, R. De Borst, An isogeometric analysis approach to gradient damage models, *International Journal for Numerical Methods in Engineering* 86 (1) (2011) 115–134.
- [17] B. Bourdin, G. A. Francfort, J.-J. Marigo, Numerical experiments in revisited brittle fracture, *Journal of the Mechanics and Physics of Solids* 48 (4) (2000) 797–826.
- [18] R. H. J. Peerlings, R. de Borst, W. A. M. Brekelmans, J. H. P. de Vree, Gradient enhanced damage for quasi-brittle materials, *International Journal for Numerical Methods in Engineering* 39 (19) (1996) 3391–3403.
- [19] G. A. Francfort, J.-J. Marigo, Revisiting brittle fracture as an energy minimization problem, *Journal of the Mechanics and Physics of Solids* 46 (8) (1998) 1319–1342.
- [20] B. Bourdin, C. P. Chukwudzie, K. Yoshioka, A variational approach to the numerical simulation of hydraulic fracturing, in: SPE Annual Technical Conference and Exhibition, Society of Petroleum Engineers, 2012, pp. SPE-159154-MS.
- [21] A. Mikelić, M. F. Wheeler, T. Wick, Phase-field modeling of pressurized fractures in a poroelastic medium, *ICES Report* (2014) 14–18.
- [22] K. Yoshioka, B. Bourdin, A variational hydraulic fracturing model coupled to a reservoir simulator, *International Journal of Rock Mechanics and Mining Sciences* 88 (2016) 137–150.
- [23] T. Wick, G. Singh, M. F. Wheeler, Fluid-filled fracture propagation with a phase-field approach and coupling to a reservoir simulator, *SPE Journal* 21 (03) (2016) 981–999.

- [24] S. Mauthe, C. Miehe, Hydraulic fracture in poro-hydro-elastic media, Mechanics Research Communications 80 (2017) 69–83.
- [25] W. Ehlers, C. Luo, A phase-field approach embedded in the theory of porous media for the description of dynamic hydraulic fracturing, Computer Methods in Applied Mechanics and Engineering 315 (2017) 348–368.
- [26] D. Culp, M. R. Tupek, P. Newell, M. H. Hubler, Phase-field modeling of fracture in CO₂ sequestration, in: 51st US Rock Mechanics/Geomechanics Symposium, American Rock Mechanics Association, 2017, pp. ARMA-2017-0644.
- [27] Y. Heider, B. Markert, Modelling of hydraulic fracturing and fluid flow change in saturated porous domains, Proc. Appl. Math. Mech. 17 (1) (2017) 95–98.
- [28] R. Span, W. Wagner, A new equation of state for carbon dioxide covering the fluid region from the triple-point temperature to 1100 K at pressures up to 800 MPa, Journal of Physical and Chemical Reference Data 25 (6) (1996) 1509–1596.
- [29] L. Ambrosio, V. M. Tortorelli, On the Approximation of Free Discontinuity Problems, Scuola Normale Superiore, 1990.
- [30] L. Ambrosio, V. M. Tortorelli, On the approximation of functionals depending on jumps by quadratic, elliptic functionals, Bollettino dell’Unione Matematica Italiana 6 (1992) 105–123.
- [31] E. Tanné, T. Li, B. Bourdin, J.-J. Marigo, C. Maurini, Crack nucleation in variational phase-field models of brittle fracture, Journal of the Mechanics and Physics of Solids 110 (2018) 80–99.
- [32] B. Bourdin, J.-J. Marigo, C. Maurini, P. Sicsic, Morphogenesis and propagation of complex cracks induced by thermal shocks, Physical Review Letters 112 (2014) 014301.
- [33] B. Bourdin, C. Chukwudzie, K. Yoshioka, A variational approach to the numerical simulation of hydraulic fracturing, in: M. Jirásek, O. Allix, N. Moës, J. Oliver (Eds.), Computational Modeling of Fracture and Failure of Materials and Structures: Proceedings of CFRAC 2013, 2013, p. 180.
- [34] H. Amor, J.-J. Marigo, C. Maurini, Regularized formulation of the variational brittle fracture with unilateral contact: Numerical experiments, Journal of the Mechanics and Physics of Solids 57 (2009) 1209–1229.
- [35] C. Miehe, M. Hofacker, F. Welschinger, A phase field model for rate-independent crack propagation: Robust algorithmic implementation based on operator splits, Computer Methods in Applied Mechanics and Engineering 199 (45–48) (2010) 2765–2778.

1
2
3
4
5
6
7
8
9
10
11
12
13
14
15
16
17
18
19
20
21
22
23
24
25
26
27
28
29
30
31
32
33
34
35
36
37
38
39
40
41
42
43
44
45
46
47
48
49
50
51
52
53
54
55
56
57
58
59
60
61
62
63
64
65

- [36] F. Javadpour, D. Fisher, M. Unsworth, Nanoscale gas flow in shale gas sediments, *Journal of Canadian Petroleum Technology* 46 (10).
- [37] F. Javadpour, Nanopores and apparent permeability of gas flow in mudrocks (shales and siltstone), *Journal of Canadian Petroleum Technology* 48 (8) (2009) 16–21.
- [38] S. A. Hosseini, F. Javadpour, G. E. Michael, Novel analytical core-sample analysis indicates higher gas content in shale-gas reservoirs, *SPE Journal* 20 (6) (2015) 1–397.
- [39] F. Civan, Effective correlation of apparent gas permeability in tight porous media, *Transport in Porous Media* 82 (2) (2010) 375–384.
- [40] U. Pillai, Y. Heider, B. Markert, A diffusive dynamic brittle fracture model for heterogeneous solids and porous materials with implementation using a user-element subroutine, *Computational Materials Science* 153 (2018) 36 – 47.
- [41] W. Zhu, C. Wei, S. Li, J. Wei, M. Zhang, Numerical modeling on destress blasting in coal seam for enhancing gas drainage, *International Journal of Rock Mechanics and Mining Sciences* 59 (2013) 179 – 190.
- [42] B. Bourdin, G. A. Francfort, J. J. Marigo, The variational approach to fracture, *Journal of Elasticity* 91 (2008) 5–148.
- [43] A. Logg, G. N. Wells, J. Hake, *DOLFIN: A C++/Python Finite Element Library*, Springer Berlin Heidelberg, Berlin, Heidelberg, 2012.
- [44] P. R. Amestoy, I. S. Duff, J.-Y. L'Excellent, J. Koster, MUMPS: A general purpose distributed memory sparse solver, in: *International Workshop on Applied Parallel Computing*, Springer, 2000, pp. 121–130.
- [45] T. Munson, J. Sarich, S. Wild, S. Benson, L. McInnes, Toolkit for advanced optimization (TAO) users manual, Tech. rep., Technical Report No. ANL/MCS-TM-322-Revision 3.5 (Argonne National Laboratory, 2014) (2014).
- [46] S. Balay, S. Abhyankar, M. F. Adams, J. Brown, P. Brune, K. Buschelman, L. Dalcin, V. Eijkhout, W. D. Gropp, D. Kaushik, M. G. Knepley, D. A. May, L. C. McInnes, R. T. Mills, T. Munson, K. Rupp, P. Sanan, B. F. Smith, S. Zampini, H. Zhang, H. Zhang, PETSc users manual, Tech. Rep. ANL-95/11 - Revision 3.9, Argonne National Laboratory (2018).
- [47] C. Bilgen, A. Kopaničáková, R. Krause, K. Weinberg, A phase-field approach to conchoidal fracture, *Meccanica* 53 (6) (2018) 1203–1219.
- [48] Z. A. Wilson, C. M. Landis, Phase-field modeling of hydraulic fracture, *Journal of the Mechanics and Physics of Solids* 96 (2016) 264–290.

- [49] C. Chukwudozie, Application of the variational fracture model to hydraulic fracturing in poroelastic media, Ph.D. thesis, Louisiana State University (2016).
- [50] E. Detournay, D. Garagash, The near-tip region of a fluid-driven fracture propagating in a permeable elastic solid, *Journal of Fluid Mechanics* 494 (2003) 1–32.
- [51] J. Hu, D. Garagash, Plane-strain propagation of a fluid-driven crack in a permeable rock with fracture toughness, *Journal of Engineering Mechanics* 136 (9) (2010) 1152–1166.
- [52] C. Miehe, M. Hofacker, F. Welschinger, A phase field model for rate-independent crack propagation: Robust algorithmic implementation based on operator splits, *Computer Methods in Applied Mechanics and Engineering* 199 (45–48) (2010) 2765–2778.
- [53] M. Ambati, T. Gerasimov, L. De Lorenzis, A review on phase-field models of brittle fracture and a new fast hybrid formulation, *Computational Mechanics* 55 (2) (2015) 383–405.
- [54] C. Miehe, F. Welschinger, M. Hofacker, Thermodynamically consistent phase-field models of fracture: Variational principles and multi-field FE implementations, *International Journal for Numerical Methods in Engineering* 83 (10) (2010) 1273–1311.
- [55] E. Detournay, A.-D. Cheng, Poroelastic response of a borehole in a non-hydrostatic stress field, in: *International Journal of Rock Mechanics and Mining Sciences & Geomechanics Abstracts*, Vol. 25, Elsevier, 1988, pp. 171–182.
- [56] Y. L. Lu, D. Elsworth, L. G. Wang, Microcrack-based coupled damage and flow modeling of fracturing evolution in permeable brittle rocks, *Computers and Geotechnics* 49 (2013) 226–244.
- [57] I. N. Sneddon, M. Lowengrub, *Crack Problems in the Classical Theory of Elasticity*, Wiley, New York, 1969.
- [58] M. F. Wheeler, T. Wick, W. Wollner, An augmented-Lagrangian method for the phase-field approach for pressurized fractures, *Computer Methods in Applied Mechanics and Engineering* 271 (2014) 69–85.
- [59] M. K. Hubbert, D. G. Willis, *Mechanics of Hydraulic Fracturing*, AAPG Special Volumes, 1972.
- [60] B. Haimson, C. Fairhurst, Initiation and extension of hydraulic fractures in rocks, *Society of Petroleum Engineers Journal* 7 (03) (1967) 310–318.
- [61] C. H. Yew, X. Weng, *Mechanics of Hydraulic Fracturing*, Gulf Professional Publishing, 2014.